Self-standing bearing capacity of symmetric circular masonry arches at finite friction: Technical handbook of physical states

Giuseppe COCCHETTI[1,2], Egidio RIZZI[2,*]

[1]Politecnico di Milano, Dipartimento di Ingegneria Civile e Ambientale,
piazza Leonardo da Vinci 32, I-20133 MILANO, Italy

[2]Università degli studi di Bergamo, Dipartimento di Ingegneria e Scienze Applicate,
viale Guglielmo Marconi 5, I-24044 DALMINE (BG), Italy

*Corresponding Author: egidio.rizzi@unibg.it

Accepted Preprint: 1 October 2025

Abstract

The present contribution concerns the issue of finite friction, in ruling self-standing bearing capacity and collapse modes of (symmetric circular) continuous masonry arches, with ideal inherent radial stereotomy. With primary reference, and as an enhancement, to classical "Couplet-Heyman problem", of least-thickness form optimization, in the realm of purely-rotational collapse solutions, finite (Coulomb) friction is herein set, and thoroughly explored, in implying the possible appearance of sliding activation. The configuration of uniform (vertical) self-weight distribution is considered, herein for the true Milankovitch-like distribution accounting for the real centres of gravity of the ideal wedge-shaped chunks of the arch. The mechanical problem is analyzed, through a full analytical approach, by deriving all physical domains, and explicitly separating safe vs. collapse states of the arch. Outcomes are eventually validated by a separate dedicated Complementarity Problem/Mathematical Programming numerical implementation, by fully consistent and illustrative results. Diverse key aspects are newly outlined, specifically for the representation of the characteristic solution variables as a function of friction and geometrical parameters, namely: (a) two- and three-dimensional state maps are analytically elucidated, specifically at variable arch opening; (b) underlying numerical data are thoroughly evaluated and reported in handbook tables; (c) catalogue arrays of arch geometries and collapse modes are systematically formed. The analytical-numerical achievements shall allow for a full understanding of the problem at hand, and synoptically form a technical compendium, in the Mechanics (statics) of masonry arches, and specific related role of finite friction, in providing crucial self-bearing structural capacity.

Keywords: (symmetric circular) masonry arches; least-thickness Couplet-Heyman problem; finite friction; collapse modes; self-bearing structural capacity.

1 Introduction

This paper delivers exhaustive physical and technical results on the issue of finite-friction effects in the classical "Couplet-Heyman" least-thickness estimation of self-supporting symmetric continuous circular masonry arches under uniform (vertical) self-weight, by systematically separating safe vs. collapse arch states.

In the wake of contemporary rational landmark contributions by Milutin Milankovitch [1, 2] and Jacques Heyman [3, 4], and based on original previous work by the present Authors [5–10] (and therein wide cited external references), the topic has recently been explored in comprehensive trilogy [11–13] (with further specific inherent literature framing, where different graphical-analytical and numerical strategies have been developed and employed [14–32], including specifically within the context of finite-friction effects [33–51]), whereby:

- In source (Part I) work [11], all governing mechanical equations were set, and analytically resolved until a very end, with a parallel numerical validation through a Complementarity Problem/Mathematical Programming (CP/MP) formulation, for the classical approximate Heyman-like uniform self-weight distribution along geometrical centreline, by delivering complete results in terms of governing and characteristic variables (half-opening angle from the crown α; thickness-to-radius ratio $\eta = t/r$; non-dimensional horizontal thrust $h = H/[(\gamma t d)\, r]$ or intrinsic non-dimensional horizontal thrust $\hat{h} = \eta h = H/(\gamma d r^2)$ at given arch characteristics: uniform specific self-weight per unit volume γ, out-of-plane depth d; angular rotational or sliding inner-joint position from the crown $\beta = \beta_r$ or $\beta = \beta_s$), and observed collapse modes, specifically at variable inherent friction coefficient or friction angle ($\mu = \tan\varphi$; $\varphi = \arctan\mu$).

- In subsequent Part II work [12], the mechanical analysis was extended, along the same lines, to the real Milankovitch-like uniform self-weight distribution accounting for the true positions of the centres of gravity of the ideal infinitesimal wedge-shaped chunks of the circular arch (ideally endowed with radial stereotomy), with a comprehensive comparison to the previous investigation, and illustration of all salient differences and outcomes.

- In additional Part III work [13], the study was enlarged toward exploring all multi-faceted features of the solution, and physical outcomes, again for the Milankovitch-like uniform self-weight distribution, by: delivering all two- and three-dimensional maps of the collapse states; analyzing extremal conditions on maximum horizontal thrust and inner-joint angular positions; discussing physical and mathematical multiplicity of the various recorded collapse mechanisms.

Within that frame, and with basic reference to its main implant, notation, equation settings, analytical/numerical strategies, and outcome illustrations, the present investigation newly forms a closing synoptic compendium, further reporting, still for the real Milankovitch-like uniform self-weight distribution, a complete panorama of the crucial resulting data, toward physical and technical appreciation and interpretation, in terms of analytical maps, tables of characteristic numerical values, representation of safe arch states and collapse modes.

Specifically, in terms of present novelty:

(a) The thickness-to-radius ratio vs. friction coefficient analytical η-μ two-dimensional map is explicitly elucidated at variable half-angle of embrace α, to show all peculiar landmark points, and iso-α curves, at given discrete α sampling, until the recorded limits of validity of the solution. The same is as well performed for the complete (η; μ, α) three-dimensional representation of safe (inner volume) vs. collapse (wrapping surface) arch states, with same sampled iso-α contour lines and planes. This overall shows how the masonry arch features and attached collapse states change at variable inherent governing physical arch parameters η, μ and α.

(b) As related to the above, pertinent numerical data are systematically perforated, from the analytical equations, and comprehensively reported in handbook tables, to assemble a sort of technical compendium, providing readable explicit values of the characteristic variables that may quantitatively be recorded underneath the plotted analytical dependencies, for immediate consultation and practical guideline, and assessment of possible arch states, in terms of physical implications and potential engineering applications.

(c) Attached specific comprehensive instances, and meaningful samples, of arch geometries, and relevant collapse modes, are also depicted for characteristic half-opening angles and friction coefficients, complementing illustrations already delivered in [11–13], to overall provide a complete panorama of the attained mechanical solution for the problem at hand, in the Mechanics (Statics) of masonry arches.

Accordingly, the paper is structured in two further sections, plus a closing one, as follows: in Section 2, two- and three-dimensional representations of the (η; μ, α) arch states are analytically derived, and elucidated at characteristic sampled α states, with associated numerical data exported to handbook technical tables; in Section 3, corresponding arch features and collapse modes are thoroughly illustrated by an original numerical CP/MP implementation and reported in a compilation of array figures of the collapse states, with an extensive discussion; in Section 4, local and global conclusions are outlined, on the whole mechanical investigation.

2 Analytical results

2.1 Governing equations

With chief reference to technical description in source trilogy [11–13], and earlier original prodromic work [5–10], the (five) mechanical equations governing the problem at hand can be expressed in two groups, of three rotational [5, 9, 10] and two sliding [7] activation equations, in terms of (five) underlying variables α, μ and η, h (or $\hat{h}$), $\beta = \beta_r$ ($\beta = \beta_s = \sqrt{h(1-h)}$ being implicitly represented through h), as reported below (see Fig. 1).

Figure 1.

Rotational activation equations [5,9,10] (see pure Fig. 1d, and mixed Figs. 1b,c):

- Relative rotational equilibrium of upper or lower half-arch portion, with respect to inner intrados hinge at angular position $\beta = \beta_r$ ($h_1 = h_L$ "Lower thrust", equilibrium from above; h_U "Upper thrust", equilibrium from below, see [20], to be derived for Milankovitch-like real uniform self-weight distribution as in [9]):

$$h = h_1 = h_L(\beta, \eta) = \frac{(2-\eta)\beta \sin\beta - 2(1-\cos\beta)\, fac_M}{2+\eta-(2-\eta)\cos\beta} \tag{1}$$

or

$$h = h_U(\alpha, \beta, \eta) = \frac{(2+\eta)\alpha \sin\alpha - (2-\eta)\beta \sin\beta - 2(\cos\beta - \cos\alpha)\, fac_M}{(2-\eta)\cos\beta - (2+\eta)\cos\alpha} \tag{2}$$

- Absolute rotational equilibrium of whole half-arch, with respect to shoulder extrados hinge, involving half-opening angle α, just through variable $A(\alpha) = \alpha\cot(\alpha/2)$:

$$h = h_2(\alpha, \eta) = A(\alpha) - \frac{2}{2+\eta}\, fac_M\ , \quad A(\alpha) = \frac{\alpha \sin\alpha}{1-\cos\alpha} = \alpha \cot\frac{\alpha}{2} \tag{3}$$

- Limit tangency condition of line of thrust (locus of pressure points) at haunch intrados in least-thickness condition (corrected from single term h_H of classical "approximate" Heyman solution [3] for η small), which can be expressed by a stationary condition:

$$h = h_e(\beta, \eta) = \underbrace{\beta\cot\beta}_{h_H} + 1 - \frac{2}{2-\eta}\, fac_M = \underbrace{\beta\cot\beta}_{h_H} - \frac{\eta}{2-\eta}\left(1 + \frac{2}{\eta}\,(fac_M - 1)\right) \tag{4}$$

Thereby, Milankovitch-like real uniform self-weight distribution factor fac_M, accounting for the true location of the centres of gravity of each theoretical infinitesimal chunk of the continuous arch, at larger radial distance $r_G = r\,(1+\eta^2/12)$ (see Fig. 1), is herein enabled ($\delta_M = 1$), with respect to Heyman-like uniform self-weight distribution along geometrical centreline ($\delta_M = 0$):

$$fac_M = \left(1 + \delta_M\ \eta^2/\,12\right)\ ; \quad (fac_M - 1) = \delta_M\ \eta^2/\,12 \tag{5}$$

Sliding activation equations [7] (see pure Fig. 1a, and mixed Figs. 1b,c):

- Sliding relation for activation of shoulder sliding joint (at angular location $\beta = \alpha$):

$$\mu = \mu_{ss}(\alpha, h) = \frac{h\sin\alpha - \alpha\cos\alpha}{h\cos\alpha + \alpha\sin\alpha} \qquad \text{or} \qquad h = h_\mu(\alpha, \mu) = \alpha\,\frac{\cos\alpha + \mu\sin\alpha}{\sin\alpha - \mu\cos\alpha} \tag{6}$$

- Sliding relation for activation of inner sliding joint (at angular location $\beta = \beta_s$), which can be expressed by a stationary condition:

$$\mu = \mu_{is}(h) = \left.\frac{(1-h)\cos\beta - \beta\sin\beta}{(1-h)\sin\beta + \beta\cos\beta}\right|_{\beta\,=\,\beta_s(h)\,=\,\sqrt{h(1-h)}} \tag{7}$$

2.2 Analytical outcomes

As in source trilogy [11–13], a main representation plane, of the relevant analytical solution, in the spirit of classical "Couplet-Heyman problem", of least-thickness form optimization, and completely extending it, to the case of finite friction, is that of main variable thickness-to-radius ratio η vs. inherent friction coefficient μ, at implicitly variable half-opening angle α of the symmetric circular masonry arch.

Four main regions of collapse states are outlined, ruled by the following attached equations, and represented in the main η-μ plane in the filled two-dimensional analytical plot with labels reported in Fig. 2:

- South-East region of **Purely-Rotational (PR)** modes with no sliding appearance at undefined (supercritical) μ:
$$h = h_{1,U} \ , \quad h = h_e \ , \quad h = h_2 \tag{8}$$

- North-West region of **Purely-Sliding (PS)** modes with no rotation appearance at undefined (supercritical) η:
$$\mu = \mu_{is} \ , \quad \mu = \mu_{ss} \tag{9}$$

- Lower inner pond region among the above of mixed **Sliding-Rotational (SR)** modes with shoulder sliding and inner rotation:
$$h = h_1 \ , \quad h = h_e \ , \quad \mu = \mu_{ss} \tag{10}$$

- Upper basin region among the above (and extreme boundaries $\eta = 2$ and $\mu \to \infty$) of mixed **Rotational-Sliding (RS)** modes with shoulder rotation and inner sliding:
$$h = h_U \ , \quad h = h_e \ , \quad \mu = \mu_{is} \tag{11}$$

  The latter is further specializing into three subregions, and one boundary segment, where $\beta_r > \beta_s$, and where $\beta_r < \beta_s$, separated by a locus with $\beta_r = \beta_s$, and a region where $\beta_r = 0$, separated by a locus with $\beta_r = 0$, showing rotational components becoming **Overturning-Sliding (OS)**, at finite friction, ruled by specialized equations:
$$h = h_U|_{\beta_r = 0} \ , \quad \mu = \mu_{is} \tag{12}$$
  and tending to **Purely-Overturning (PO)** at an infinite friction coefficient on Far-East limiting vertical segment at $\mu \to \infty$, for $148.44° \simeq \alpha_l \leq \alpha \leq \alpha_L \simeq 151.74°$.

These four main domain regions are separated by curvilinear South-West/North-East dorsals, intertwining at characteristic watershed Triple point T, where the regions are directly pinned, among each other (with four co-present physical PS/RS/SR/PR collapse mechanisms, as illustrated in Fig. 1, though with demonstrated kinematic multiplicity three [13]), then showing further peculiar landmark points, i.e. Shift point S, Junction point J and Border point B, along the upper divide separating Purely-Sliding modes and mixed Rotational-Sliding modes (Fig. 2).

In the inner pond region below-left from Triple point T, there also appear peculiar stationary points where intrinsic non-dimensional horizontal thrust $\hat{h}$ is locally maximum, and where rotational/sliding angular positions from the crown $\beta_{r,s}$ are locally maxima (issues specifically investigated and revealed in [13]).

Figure 2.

2.3 Scanning at variable arch opening

All this is further illustrated in the characteristic two-dimensional η-μ analytical plot with landmark points reported in Fig. 3, where corresponding characteristic iso-α values (approximate, in deg) are depicted, showing the spacing of the collapse modes at increasing variable half-opening angle α from below.

Thereby, coming from the right, at $\mu \to \infty$, by going to a reducing, finite μ, below the asymptote limit for Purely-Rotational solutions at $\eta_l = 2(2\sqrt{3} - 3) \simeq 0.9282$, for $\alpha_l \simeq 148.44°$ ($A_l = \sqrt{3} - 1 \simeq 0.732$), horizontal lines at constant η hit a sliding border of mixed modes, get inclined, at rising η and lowering μ, then become vertical, at constant μ and undefined η, for Purely-Sliding modes.

Further, among the asymptotes at limit $\alpha_l \simeq 148.44°$ ($A_l = \sqrt{3} - 1$) and Limit $\alpha_L \simeq 151.74°$ ($A_L = 2/3$), of validity of the solutions, hyperbola-like curves directly re-join the transition from infinite to finite μ, at increasing η, reaching the upper dorsal up to Border point B, and then physical border $\eta = 2$ ($t = 2r$), at variable μ and α.

The characteristic α-lines, leading to the markers of the above-mentioned stationary points, and their transitions, at variable η and μ, are also shown, to depict the paths leading to such stationary points, and to highlight the hierarchy in terms of half-opening angle α, increasing in finding first β_s^{max}, then $\hat{h}^{max}$ and finally β_r^{max} (on such stationary points, see specifically [13], and prodromic purely-rotational [10]).

Additionally, Fig. 4 reports the same η-μ analytical plot, with further systematic scanning of discrete, constant-stepped iso-α values, and relevant level curves, namely:

- Below watershed Triple point T, for first nine α values between 50° and 130°, each 10°, namely:

$$\alpha = 50°,\ 60°,\ 70°,\ 80°,\ 90°,\ 100°,\ 110°,\ 120°,\ 130° \tag{13}$$

- Above watershed Triple point T, for other nine α values between 140° and 148°, each 1°, namely (notice the much narrower angular range):

$$\alpha = 140°,\ 141°,\ 142°,\ 143°,\ 144°,\ 145°,\ 146°,\ 147°,\ 148° \tag{14}$$

- Nearing Border point B, and beyond, for further three α values between $\alpha_l \simeq 148.44°$ and $\alpha_L \simeq 151.74°$, again each 1°, of directly asymptotic hyperbola-like iso-α lines, namely:

$$\alpha = 149°,\ 150°,\ 151° \tag{15}$$

This reveals a complete map of the η-μ values, as coupled to the source α values, in the whole range of validity of the mechanical solution, i.e. for $0 \leq \alpha \leq \alpha_L \simeq 151.74°$.

Figures 3-4.

Furthermore, the relevant "exact" numerical data, of all the characteristic arch variables, are systematically perforated, with up to 16 significative digits (though the last one or last couple of ones may result uncertain, from the numerical find-root processes needed to resolve the involved transcendental equations), from the arrays of the governing mechanical equations, along the above-mentioned scanned α values, at commanding α and μ (or φ), and gathered in handbook Tables 1-5, for direct quantitative inspection and evaluation, forming a true technical catalogue for prompt consultation, also in view of practical applications:

- As per the selected nine α values in Eq. (13), Tables 1-2 concern the double points involved with Sliding-Rotational appearance, below-left from watershed Triple point T, respectively on the lower ss and upper is borders of the inner pond.

- As per the selected nine α values in Eq. (14), Tables 3-4 concern the double points involved with Rotational-Sliding or Overturning-Sliding appearance, above-right from watershed Triple point T, respectively on the lower is and upper ss borders of the upper basin.

- As per the selected further three α values in Eq. (15), Table 5 concerns single/double points involved with Overturning-Sliding appearance, between the asymptotes for $\alpha_l \simeq 148.44^\circ$ ($\eta_l \simeq 0.9282$) and $\alpha_L \simeq 151.74^\circ$ ($\eta_L = 2$).

Remark 1 (on conservative SAFE-state estimation)

Notice that the values of friction coefficient μ (or friction angle φ) and thickness-to-radius ratio η listed in Tables 1 and 3, at variable reference half-opening angle α, referring to the lower shoulder sliding/inner sliding ss/is dorsals that bound from the left the Purely-Rotational collapse states, practically provide lower-bound estimates, of friction and geometrical thickness parameters, to allow stating that the masonry arch is anyway SAFE, within the plane quadrant with μ and η larger than the reported values, at each considered α.

This provides a direct conservative estimate of self-standing bearing capacity of the symmetric circular masonry arch at variable inherent friction.

Tables 1-5.

2.4 Three-dimensional state representations

To conclude the analytical analysis, wider, complete three-dimensional representations of the masonry arch states in terms of physical underlying governing variables (η; μ, α) are depicted in Figs. 5-6, the latter reporting as well iso-α contour lines and planes, for the above-considered scanned values of half-opening angle α in Eqs. (13)-(15), first each 10° below watershed Triple point T and then each 1° above it, overall showing that:

- The safe self-standing states of the circular masonry arch are those corresponding to the inner volume underneath the external surface of the collapse states, with the various folds linked to the different collapse modes, which, projected onto the η-μ plane, delivers the η-μ two-dimensional plots in Figs. 2-4;

- Any inner safe arch state, for instance laying on a given α = const plane, may be brought to incipient collapse, with the different possible collapse manifestations, by paths reaching the surface envelope, for instance, moving on the α = const plane, by η = const or μ = const, or with both variable parameters η and μ, or by other paths, which may directly change three variables (η; μ, α) all together, leading to a specific collapse configuration of the masonry arch;

- Like that, with similarity, for instance, to classical Strength of Materials or Theory of Plasticity, the original "Couplet-Heyman concept", of least-thickness form optimization, herein goes much beyond, in completely separating safe and collapse states, showing that the volume inside the surface, of safe arch states, looks like a strength or yield domain, and the wrapping surface around it appears like a strength or yield limit, then marking the arch states that are prone to incipient collapse, accounting for the various PS/RS/SR/PR collapse manifestations;

- Though the conceptual (η; μ, α) three-dimensional state representation is the clearer, and more complete one, it provides a more qualitative depiction, than the quantitative one represented by the (η, μ) two-dimensional description, with attached data that have systematically been gathered in numerical tables (Tables 1-5), to deliver, all together, a clear technical map and complete catalogue of the possible arch states, also in view of potential practical implications and engineering applications.

Figures 5-6.

The formed novel and systematic information becomes complementary to that earlier provided in source trilogy [11–13], and should then be appreciated all together, to provide a complete panorama of the various physical manifestations of the achieved mechanical solution and to form a sort of technical handbook toward practical interpretations and architectural/engineering applications.

3 Numerical illustration

An original, Complementarity Problem/Mathematical Programming (CP/MP) formulation and numerical implementation [8, 9] is then systematically employed to corroborate and illustrate the various characteristic arch states at variable half-opening angle α, as considered in previous Section 2, herein again for the true Milankovitch-like uniform self-weight distribution (Fig. 1), which can conveniently be flagged on, within the numerical procedure, as analytically detailed in Section 2.1.

The numerical CP/MP formulation has extensively been introduced in [8], and later updated in [9], references to which the interested reader may be referred to, for the various technical details. As a main general concept, and as typically outlined in the Theory of Plasticity, of Solids and Structures, and in Limit Analysis, masonry arch states can be handled by setting a Complementarity Problem, among strength conditions within static internal variables $\boldsymbol{\varphi}$ and collapse kinematic variables at rotating/sliding joints $\dot{\boldsymbol{\lambda}}$.

This may further be brought down to a Mathematical Programming (minimization) problem, under linear constraints, herein with apparent arch collapse onset that may numerically come out in the order of 10^{-16}, for targeted objective function $-\boldsymbol{\varphi}^T \dot{\boldsymbol{\lambda}}$, in the quest of a true numerical zero for the sought minimum extremal condition:

$$\textbf{CP:} \quad \boldsymbol{\varphi} \leq \mathbf{0} \,, \quad \dot{\boldsymbol{\lambda}} \geq \mathbf{0} \,, \quad \boldsymbol{\varphi}^T \dot{\boldsymbol{\lambda}} = 0 \tag{16}$$

$$\Downarrow$$

$$\textbf{MP:} \quad \min \Big\{ -\boldsymbol{\varphi}^T \dot{\boldsymbol{\lambda}} \,|_{\,lin.\ constr.} \Big\} = 0 \tag{17}$$

Such a "φ-λ formulation" turns out particularly feasible, in the present setting of tracing masonry arch mechanisms, to locate and depict the collapse modes that are reached in the least-thickness condition, at given geometrical morphology and variable inherent friction among the theoretical blocks of the arch, coming from the characteristic features that are "exactly" calculated by the analytical solution, as described in Sections 2.1-2.2. The numerical strategy then allows to validate the analytically-obtained input characteristic data, for the various morphologies and inherent properties of the masonry arch, and consents to illustrate, all together: geometrical properties in the reference configuration (black); static features in terms of "line of thrust" (red) and "line of friction" (blue); kinematical appearances in the shape of recorded (symmetric) collapse mechanism (green).

Herein, notice that the *"line of thrust"* is classically taken as the locus of pressure points, of non-dimensional eccentricity $\hat{e} = [M/N]/[t/2] = e/[t/2]$, i.e. moment over axial compression force ratio within the arch, normalized to be ± 1 at a rotational joint activation [5], and the *"line of friction"* is originally meant as the locus of shear over normal force ratio, normalized as $\hat{e}_s = [T/N]/\mu = e_s/[t/2]$ to be ± 1 at a sliding joint activation [8]. Then, when such lines come to touch the intrados or extrados of the masonry arch, (radial) failure joints are thereby activated, within the arch, to possibly deliver a collapse mechanism as coherently described by compatible kinematic variables $\dot{\boldsymbol{\lambda}}$ complementary to underlying conformal static variables $\boldsymbol{\varphi}$, as per Eq. (16), which truly separates safe vs. collapse arch states.

3.1 Arrays of collapse states

According to the previous description in preceding Section 2, macro-illustration graphical arrays are systematically formed to the handbook purpose in Figs. 7-15, to provide a comprehensive overview of arch features and collapse states at variable half-opening angle α of the masonry arch, and inherent friction. Specifically, also referring to numerical data already perforated in Tables 1-5:

- The frames in Figs. 7-10 gather the views of the arches linked to the double points at the boundaries of the inner pond region of mixed Sliding-Rotational modes, with shoulder sliding and inner rotation, occurring below-left from Triple point T, for variable α between 50° and 130°, each 10°, showing both undercomplete arches ($\alpha < 90°$) and overcomplete arches ($\alpha > 90°$), separated by the complete semicircular arch case ($\alpha = 90°$). In practice, the collapse modes that are concomitantly present at those double points are shown, at chosen variable α, and associated η-μ interface values.
  - Within that, the frame in Fig. 7 shows the Purely-Rotational (PR) modes at the lower interface for shoulder sliding (ss) activation; the frames in Fig. 8 and 9 depict the mixed Sliding-Rotational (SR) modes at the lower (SR^-) and upper (SR^+) interfaces, respectively with shoulder sliding (ss) and inner sliding (is) activation; the frame in Fig. 10 displays the Purely-Sliding (PS) modes at the upper (is) interface of the inner pond region.

- The frames in Figs. 11-14 similarly gather the arches tied to the double points of the upper basin of mixed Rotational-Sliding modes, with shoulder rotation and inner sliding, occurring above-right from Triple point T, for variable α between 140° and 148°, each 1°, referring to overcomplete arches that anyway display a half-opening angle lower than the first asymptotic limit of $\alpha_l \simeq 148.44°$ first leading to Purely-Overturning at $\mu \to \infty$.
  - Within that, the frame in Fig. 11 shows the Purely-Rotational (PR) modes at the lower interface for inner sliding (is) activation; the frames in Fig. 12 and 13 depict the mixed Rotational-Sliding (RS) modes at the lower (RS^-) and upper (RS^+) interfaces, respectively with inner sliding (is) and shoulder sliding (ss) activation, becoming Overturning-Sliding with and above $\alpha = 146°$; the frame in Fig. 14 displays the Purely-Sliding (PS) modes at the upper (ss) interface of the upper basin region.

- The frame in Fig. 15 finally gathers the arches linked to the single/double points of the upper basin of Overturning-Sliding modes, occurring among asymptotic limits $\alpha_l \simeq 148.44°$ and $\alpha_L \simeq 151.74°$, for the three α values of 149°, 150° and 151°.
  - Within that, the above row of the frame shows Purely-Overturning (PO) modes at $\mu \to \infty$; the middle row displays mixed Overturning-Sliding (OS) modes (for case $\alpha = 151°$, as recorded at hitting upper physical border $\eta = 2$ with $t = 2r$); the bottom row depicts Purely-Sliding (PS) modes, just for $\alpha = 149°$ and 150° (case $\alpha = 151°$ being unable to reach Purely-Sliding modes due to the hitting of upper border $\eta = 2$), and (in place of that, to fill the array), the Purely-Overturning mode at $\mu \to \infty$ and $\eta = 2$, for Limit angle $\alpha_L \simeq 151.74°$.

Figures 7-15.

3.2 Sample safe vs. mixed collapse states

Moreover, two groups of additional selected illustration instances are considered, in order to show the transition from a safe state of the arch to a (mixed) incipient collapse mode, either Sliding-Rotational (SR) or Rotational-Sliding (RS), which may appear for a given physical arch state, in terms of assigned (rounded or almost rounded) physical variables, i.e. thickness-to-radius ratio η, inherent friction coefficient μ (or friction angle φ) and half-opening angle α.

To the purpose, two meaningful groups of four sample cases are considered (with rounded values, in the collapse states, for two out of the three governing variables, with the resulting critical value for the third one, to induce mixed collapse), as shown in 2×2 array Figs. 16-17, with main characteristic data in Tables 6-7, corresponding to points in the η-μ plane in Figs. 2-4 that result almost in the middle of the rising non-linear curves among sliding activation boundaries, at increasing η, with lowering μ, either below-left or above-right from watershed Triple point T, respectively into the inner pond of mixed Sliding-Rotational modes or into the basin of mixed Rotational-Sliding modes, namely:

- A group that displays η around 0.5, μ around 1.0 (φ around 45°), α around 130°, potentially leading to SR collapse, as set out by equations $h = h_L$, $h = h_e$, $\mu = \mu_{ss}$ in Eq. (10), where the use of Lower thrust h_L and shoulder sliding activation on μ_{ss} should be noticed (see resulting arch illustrations in Fig. 16, and characteristic data in Table 6 and below text);
- A group that displays η around 0.8, μ around 1.8 (φ around 61°), α around 145°; potentially leading to RS collapse, as set out by equations $h = h_U$, $h = h_e$, $\mu = \mu_{is}$ in Eq. (11), where the use of Upper thrust h_U and inner sliding activation on μ_{is} should be noticed (see resulting arch illustrations in Fig. 17, and characteristic data in Table 7 and below text).

The resulting masonry arch states for the first group with rather self-similar SR collapse manifestations are illustrated in 2×2 array Fig. 16, where the four shots show:

- (a) SAFE state, for the reference value of $\alpha = 130°$ and given rounded $\eta = 0.5$, $\mu = 1.0$ ($\varphi = 45°$) reference state. Thereby, a possible configuration of line of thrust and of line of friction is drawn, for the continuous arch, safely included within it, minimizing objective function $-\boldsymbol{\varphi}^T \dot{\boldsymbol{\lambda}}$, though to a non-zero positive value, thus by excluding collapse;
- (b) Mixed SR collapse state, for that given rounded $\eta = 0.5$, $\mu = 1.0$ ($\varphi = 45°$) reference state, at the resulting critical α value, around $\alpha \simeq 130°$, namely $\alpha = 2.270495186553218 \simeq 130.09°$, with resulting $h = 0.1950576155171495$, $\hat{h} = \eta h = 0.09752880775857475$ and $\beta_r = 1.104208246586004 \simeq 63.27°$;
- (c) Mixed SR collapse state, for that given rounded $\eta = 0.5$ and half-opening $\alpha = 130°$, for $\mu = 0.9969880290274362$ ($\varphi \simeq 44.91°$), with resulting $h = 0.1950576155171495$, $\hat{h} = \eta h = 0.09752880775857475$ and $\beta_r = 1.104208246586004 \simeq 63.27°$ (values of h, $\hat{h} = \eta h$ and β_r in (b) and (c) are the same, since recorded with arising inner-joint rotation at same $\eta = 0.5$, despite at slightly different α values, within Eq. (10));
- (d) Mixed SR collapse state, for that given value of $\mu = 1.0$ ($\varphi = 45°$) and half-opening $\alpha = 130°$, for $\eta = 0.4953913040890266$, with resulting $h = 0.1985054807705899$, $\hat{h} = \eta h = 0.09833788898776172$ and $\beta_r = 1.105603069270766 \simeq 63.35°$.

Figure 16 and Table 6.

The resulting masonry arch states for the second group with rather self-similar RS collapse manifestations are illustrated in 2×2 array Fig. 17, where the four shots show:

- (a) SAFE state, for the reference value of $\alpha = 144°$ and given rounded $\eta = 0.8$, $\mu = 1.8$ ($\varphi \simeq 61°$) reference state. Notice that the arch is safe for $\alpha = 144°$, while it is not for $\alpha = 145°$. Thereby, again, a possible configuration of line of thrust and of line of friction is drawn, safely included within the continuous arch, minimizing $-\boldsymbol{\varphi}^T \dot{\boldsymbol{\lambda}}$, though to a non-zero positive value, ruling out collapse;

- (b) Mixed RS collapse state, for that given rounded $\eta = 0.8$, $\mu = 1.8$ ($\varphi \simeq 61°$) reference state, at the resulting critical α value, around $\alpha \simeq 145°$, namely $\alpha = 2.526201114497218 \simeq 144.74°$, with resulting $h = 0.06573404085108929$, $\hat{h} = \eta h = 0.05258723268087143$ and $\beta_r = 0.7192773522588299 \simeq 41.21°$, $\beta_s = 0.2478166191450376 \simeq 14.20°$;

- (c) Mixed RS collapse state, for that given rounded $\eta = 0.8$ and half-opening $\alpha = 145°$, for $\mu = 1.936371249842161$ ($\varphi \simeq 62.69°$), with resulting $h = 0.05793516577873266$, $\hat{h} = \eta h = 0.04634813262298612$ and $\beta_r = 0.7342349796084060 \simeq 42.07°$, $\beta_s = 0.2336208088868015 \simeq 13.39°$ (values of h, $\hat{h} = \eta h$ and β_r in (b) and (c) are not the same, since recorded with arising inner-joint sliding, at β_s, even if at same $\eta = 0.8$ and at slightly different α values, within Eq. (11));

- (d) Mixed RS collapse state, for that given value of $\mu = 1.8$ ($\varphi \simeq 61°$) and half-opening $\alpha = 145°$, for $\eta = 0.8170487848718171$, with resulting $h = 0.06573404085108929$, $\hat{h} = \eta h = 0.05370791820209689$ and $\beta_r = 0.6598405767270294 \simeq 37.81°$, $\beta_s = 0.2478166191450376 \simeq 14.20°$ (values of h and β_s in (b) and (d) are herein the same, since recorded with arising inner-joint sliding at same μ, as per inner-sliding activation Eq. (7), within Eq. (11)).

Figure 17 and Table 7.

In finally mutually commenting the visual outcomes linked to SR vs. RS illustration Figs. 16 and 17:

- Both SR and RS collapse manifestations, in three frames (b), (c), (d), for each figure, result very similar, among themselves, given the rather near values of underlying physical parameters (η; μ, α);

- However, each frame (a) in the two figures highlights a safe state of the arch, again for slightly different values, of the underlying arch parameters. This shows that, being the assumed rounded reference states quit near to the 3D collapse surface in Figs. 5-6, the arch is still safe, in a slightly subcritical condition, (a), then becoming critical, (b) to (d), for a slight, though precise variation of (even one of) the governing parameters;

- A little wider difference, in the characteristic parameters, and resulting manifestations, is recorded for the SR reference state around 145°, since thereby a higher variation within the iso-α stepping has been recorded, in 2D Fig. 4 and 3D Fig. 6;

– Also, thereby notice that while $\alpha = 130°$ is safe, with respect to SR modes, Fig. 16(a), $\alpha = 145°$ is not, with respect to RS modes, namely leading to a supercritical condition, and then nearer rounded inferior value $\alpha = 144°$ has been considered, Fig. 17(a); indeed, while $\eta \simeq 0.49539$ is subcritical to $\eta = 0.5$, in Table 6, $\eta \simeq 0.81705$ is supercritical to $\eta = 0.8$, in Table 7. Thus, while frames (a), (c), (d) in Fig. 16 are drawn for $\alpha = 130°$, only frames (c), (d) in Fig. 17 are depicted for $\alpha = 145°$, (a) being shown for $\alpha = 144°$, while both frames (b) in Figs. 16 and 17 are depicted for the slightly different critical values of α, at the given rounded η-μ state, slightly larger than those, rounded ones, taken for the safe arch states in frames (a).

3.3 Discussion

The present discussion is now set, about various issues and remarks that have arisen at review stage, which may be useful to be shared, for the appreciation of the overall investigation, by the final general and specific readers.

► **About the collocation and value of the present manuscript**, this is a sort of closing compendium of recent trilogy [11–13], as the output of a comprehensive research project, focussed on the issue of finite friction, in the Mechanics (Statics) of (continuous symmetric circular) masonry arches under uniform (vertical) self-weight, generalizing the so-called "Couplet-Heyman" problem of least-thickness form optimization, and going much beyond that.

It comes after prodromic self-works [5–10], which have mainly analyzed the role of classical purely-rotational solutions [5, 6, 9, 10] and started the investigation on the possible sliding onset [7, 8]. As a structural paradigm, given the content, one may say this paper to constitute a "keystone", set at the crown of the arch, made of the chunks constituted by such previous papers, which may be necessary, for a full understanding of the various subtleties, and for potential self-replication of the present results. So, they bare on each other, conceptually, to stand overall, and be appreciated all together.

Positioning to previous Parts I-III [11–13] is stated in the first itemized list in the Introduction. Novelty is formulated in the (a), (b), (c) list in Abstract and Introduction. Accordingly, main novelty is constituted, as technical content, by Figs. 3-4, Tables 1-5, and Figs. 7-15, to form a comprehensive catalogue of arch states. This shall be unprecedented, in the literature (documented and extensively discussed in such previous works, and herein [14–51], with various contributions that have analysed the research topic, specifically about the role of finite friction [33–51]), and should state the conceptual value of the present research, also in practical terms (see also Remark 1, on the minimum amount of friction necessary to avoid sliding, quantitatively formalizing the value of 3rd Heyman hypothesis of no sliding failure).

Additionally, Figs. 5-6, and text in Section 2.4, finally form the concept of "safe domain", in the space of arch variables, as in Strength of Materials or Theory of Plasticity, going much beyond the main source "Couplet-Heyman problem" least-thickness form optimization context. This is also something relevant for the appreciation of the amount of constitutive friction, as related to morphological arch opening, and thickness.

► **About the positioning to previous attempts in the literature**, specifically concerning the role of finite friction, in masonry arches and structures [33–51], while other preliminary contributions have provided partial results (e.g. [35, 36, 40]), on specific configurations, and in some cases in different ones, as that considered in this work, this investigation, for the considered configuration, systematically traces all possible solutions, for all ranges of the underlying variables, providing a clear and comprehensive picture of the whole, and of the underlying single cases, setting up a general frame, which should clear the picture, on the role of finite friction, in the self-standing capacity of uniform (symmetric circular) masonry arches.

Outcomes shall also be useful in general terms, and instructive, even in handling, by extrapolation, other arch geometries and loading settings, as for instance considering unsymmetric or different geometrical shapes of the masonry arch [23, 25, 29, 38, 47], issues of stereotomy (i.e. the shape of the stone cuttings of the mutual joints of voussoir arches [4, 28, 30, 31, 50]), effects of boundary conditions [22], different loading configurations (e.g. including lateral actions [22, 26, 38]), and so on.

► **About the effective use of the present outcomes**, for studying the Mechanics (Statics) of an existing circular arch, one may first notice that several sample cases were already studied and extensively illustrated in previous Part I-III papers [11–13].

Moreover, the instances herein explicitly considered to the purpose in Section 3.2, with results in Fig. 16/Table 6 and Fig. 17/Table 7, were indeed meant in the above sense, in order to show a possible transition from a safe state of the arch to a (mixed) incipient collapse mode, either Sliding-Rotational (SR) or Rotational-Sliding (RS). Hopefully, these outcomes should be clear, overall, to the end readers.

► **About the practical utilization of Tables 1-5**, in the Statics of (symmetric circular) masonry arches, the following could be said.

One may "enter the table" with a given half-opening angle α of the circular arch (herein scanned in deg).

Then, one first reads the values of friction coefficient μ or friction angle φ that provide the critical friction state considered for each table (for instance, in Tables 1 and 3, about the critical threshold to sliding activation, respectively at the shoulder or at an inner joint). Friction values larger than that would then prevent those forms of failure, with sliding, from appearing, within the masonry arch.

Next, the value of least thickness-to-radius ratio η in the critical condition is accessed, providing a measure of the thickness that the arch, at least, should possess, to be possibly withstanding, its uniform self-weight.

Further, the values of non-dimensional horizontal thrusts h and $\hat{h} = \eta h$ arising within the arch (normalized static quantities) can be appreciated, in order to estimate the amount of push that the arch may bring down to the shoulders, in the critical condition, at incipient collapse, for the structural evaluation of the supporting abutments.

Finally, the angular positions of rotational and/or sliding joints, β_r and β_s, are decipherable, toward comprehending the morphological characteristics of the failure modes and localizing the joints that may likely be exposed to failure (or possibly be strengthened, to prevent collapse, for instance by placing ties), specifically once the arch is not a continuous one (which ideally opens

up the rupture joints where it is needed), rather a discrete one made by real chunks, with failure joints that may be the nearer to the analytically-determined ones, for a continuous arch (notice that, though, a comprehensive analysis for discrete arches is out of the scopes of the present contribution, devoted to continuous arches, and may be the subject of further specific attention).

► **About the representation of the half-opening angle**, notice that in Figs. 5-6, half-opening angle α is expressed in rad, as a primary real variable, in the source calculations, as per other non-dimensional variables η and μ, and as earlier done in prodromic Parts I-III [11–13].

However, the subsequent scanning of α values has been selected in deg, for easier and practical interpretation (Section 2.3). Anyway, in Tables 1-5 and text, α values in rad are as well provided.

► **About the assumption of the loading condition**, the developed analytical solution, and numerical validation, is indeed rather peculiar, given the supposed uniform (vertical) self-weight distribution. In the considered setting, of symmetric circular masonry arches, this allows for a convenient handling and to achieve explicit solutions, which, in general, may not apply, for other arbitrary loading configurations that one may consider.

However, in other loading cases, the conceptual reasoning would likely be the same, so that the issue of minimum arch thickness, and, most of all, that of safe domain, for the arch states, as delivered in the paper, may still be obtained, for a given, specific loading configuration that may be imagined.

Despite, in case that loads may be independent, as accidental or concentrated ones, from arch thickness, as herein considered, in the sense that uniform self-weight loading is brought in through thickness-to-radius ratio η, as physical variable (to be minimized), within the underlying Limit Analysis framework, instead of expressing an explicit load multiplier (to be statically maximized), this may reflect in a different key of reading, of the core outcomes, though the main conceptual implant could also be the same, or, say, a similar one.

So, extensions to other loading configurations (even with other self-weight distributions, e.g. with the presence of non-vertical components) may not be straightforward, in general, and would anyway open up the way to separate, specific, analytical handlings, whenever possible, for each specific loading condition.

In that, the scheduled subsequent numerical treatment, by the CP/MP formulation, once adopted to handle specific given loadings, may instead display further potentialities, also in representing particular loading configurations that may appear in real cases, even considering discrete arches with given arch and chunks morphologies, all this constituting a pertinent scenario, though going much beyond, the present setting of continuous circular arches under uniform self-weight, but that in principle could numerically be handled, in perspective.

► **About the meaning and value of the present numerical CP/MP formulation**, mainly, one shall first say that, so far, the present adoption, of such a self-assembled numerical procedure, is hierarchically subordinated to the role and use of the derived analytical solution, in the considered setting.

Thus, through the analytical derivation, the basic underlying arch variables are calculated (by "exact" values, with a good number of significative digits; this is why several digits are reported in text and numerical tables, as necessarily needed, to arrive at a true numerical zero,

in the $-\boldsymbol{\varphi}^T \dot{\boldsymbol{\lambda}}$ minimization process, in case of reaching a true collapse condition).

Next, arch characteristics (values of thickness-to-radius ratio η and friction coefficient μ, number of blocks and angular positions of the failure joints, β_r and β_s, at given half-opening angle α) are transferred to the numerical tool, to validate the analytical solution (and allow for the concomitant representation of arch configuration, lines of pressure and of friction, and collapse mode, for illustration purposes).

So, in that sense, the numerical tool, so far, is not meant to be completely "predictive", in finding out by itself the configurations that would lead to collapse (several trials could be made, for instance iteratively, but with difficulties in chasing the real arch morphology and collapse configuration) and herein is basically adopted in confirming the expected arch state, after setting in input the "exact" arch features that implacably arise from the analytical solution.

Moreover, as it may be noticed, given that the set of equations governing the mechanical problem is a non-linear one, and that in the resulting numerical CP/MP optimization approach a non-convex objective function is present, by product $-\boldsymbol{\varphi}^T \dot{\boldsymbol{\lambda}}$, on the issue of potential (non-)uniqueness of the optimization solution, the following considerations may be in order.

Remarks on uniqueness of the optimization solution

The non-linear CP/MP formulation is herein specifically devised to validate, for given geometrical quantities and friction coefficient of the masonry arch, the analytical solution (based only on static equations). Specifically, in the 3D space of underlying variables thickness-to-radius ratio η, friction coefficient μ, half-opening angle α, as per the 3D representations in Figs. 5-6:

1) Within the physical domain, it results $\min\{-\boldsymbol{\varphi}^T \dot{\boldsymbol{\lambda}}\} > 0$ (see also the extensive iso-contour representations provided in source numerical paper [8]). This means that it is possible to fulfil both equilibrium and compatibility, but that they are not "coherent", with "constitution", i.e. with the complementarity requirement among static and kinematic variables. From the mechanical point of view, no collapse solutions are admitted. The arch is then safe.

2) On the domain surface, orthogonality holds as $\min\{-\boldsymbol{\varphi}^T \dot{\boldsymbol{\lambda}}\} = 0$, where 0 is a numerical zero, e.g. in the order of 10^{-16}. Then, all the equations governing the collapse state are satisfied, i.e. at least one collapse mechanism is foreseen for the tested geometrical configuration and the given friction coefficient. This represents incipient collapse of the arch, in the reached critical condition, in the classical sense of Limit Analysis.

3) Outside the physical domain, no feasible solutions are obtained (i.e. the solution of the optimization problem turns out computationally "unfeasible"). Thus, it is not possible to satisfy equilibrium and/or compatibility, being the violation, in general terms, relevant to the source equilibrium relations. Mechanically speaking, a dynamic collapse takes place, namely the arch is not able to withstand its self-weight.

In a strict mathematical sense, no uniqueness is expected for the collapse configurations. Indeed, this is clearly true, for specific cases:

– For instance, in the Purely-Rotational case, at supercritical or infinite friction, only one set of static redundants, in the doubly-built-in arch [8], is found, but a "ray solution" is

obtained for the kinematic variables, describing the collapse mechanism, being the (physically same) failure mode possibly be amplified by an arbitrarily defined positive factor.

– Another clear example of non-uniqueness is represented by the Purely-Sliding collapse case, at any arbitrary supercritical thickness-to-radius ratio, ruled just by translational static equations, where besides the arbitrarily defined positive factor amplifying the mechanism, also a redundant moment, in the doubly-built-in arch [8], can arbitrarily be chosen within an interval.

– Further, multiple mechanisms can appear (for instance, on the border of contiguous regions of the 2D and 3D state maps in Figs. 2-4 and 5-6), and the positive amplification factors become more than one, though kinematic variables $\dot{\boldsymbol{\lambda}}$ may arbitrarily be normalized, e.g. by a constraint of unit norm, also to prevent falling on trivial solution $\dot{\boldsymbol{\lambda}} = \mathbf{0}$ [8]. Incidentally, the multiplicity of the failure mechanisms, specifically at watershed Triple point T in the 2D analytical maps in Figs. 2-4, where multiplicity is demonstrated to result mathematically triple, while it appears physically quadruple, with four concomitant physical collapse modes (see Fig. 1), has widely been studied in a dedicated section in Part III [13].

– Despite, there have not appeared cases of "physical" non-uniqueness, even considering the possible effect of non-normality, linked to finite-friction effects, in the underlying framework of Limit Analysis (as widely discussed in Part II), in the practice of the handling of the CP/MP formulation (still in the present setting of symmetric masonry arches), as used, after known values from the analytical solution, showing much robust, in predicting collapse, "exactly", with a numerical zero in the order of 10^{-16}, once imputed arch characteristic values become truly "exact".

– In short, heuristically, besides the instances in which non-uniqueness is intrinsically, physically expected, no signs of non-uniqueness have emerged, in the managing of the CP/MP optimization procedure, which turns out rather reliable, in the considered setting of symmetric circular arches under uniform (vertical) self-weight.

4 Conclusions

The present research investigation shall complement the wide mechanical analysis on finite-friction effects in (symmetric circular) continuous masonry arches under uniform (vertical) self-weight developed in source trilogy [11–13], by providing further crucial analytical and numerical results, specifically in view of elucidating an explicit connection to the variation of half-opening angle of the arch α, and the link to inherent friction coefficient μ, and forming a synoptic compendium and technical handbook, for direct understanding and utilization.

Clearly:

- Watershed Triple point T in the η-μ map separates the main (wider and common) range of half-opening angles α lower than about 139.23°, say around 140°, and the rather narrow range of half-opening angles higher than that and up to the upper limit of about 151.74°, say around 152°, thus of only about further 12°.

- In the former case, mixed collapse modes may arise, in the form of mixed Sliding-Rotational modes, with sliding at the shoulder and inner rotation, below-left from watershed Triple point T, representing the cushion, inner pond region in between Purely-Rotational and Purely-Sliding modes.

- In the latter case, mixed collapse modes may arise, in the form of mixed Rotational-Sliding modes, with rotation at the shoulder and inner sliding, above-right from watershed Triple point T, even representing, after a half-opening angle α at about 145°, leading to Junction point J, Overturning-Sliding modes with inner sliding or even Purely-Overturning modes just at infinite friction ($\mu \to \infty$; $\varphi \to 90°$).

- Notice that friction coefficients/angles higher than the characteristic values recorded at watershed Triple point T ($\mu \simeq 1.277$; $\varphi \simeq 52°$) shall prevent any mixed Sliding-Rotational mode to appear, while friction values higher than those recorded at Border point B at physical limit $\eta = 2$ with $t = 2r$ ($\mu \simeq 1.854$; $\varphi \simeq 62°$) shall prevent any Purely-Sliding mode to arise within the arch. This shall quantify, in general terms, the amount of required friction to comply with classical third Heyman [3] hypothesis of no sliding failure.

- Moreover, as an important remark (see Remark 1 at the bottom of Section 2.3), as per the values of μ and η listed in Tables 1 and 3, for the various half-opening angles α, linked to the lower ss/is dorsals in the η-μ plane, these provide consistent and conservative lower-bound estimates warranting the safe state of the arch for any η-μ plane quadrants with larger values of η and μ, at each given α.

- The interaction among increasing half-opening angle α and rising friction coefficient μ useful for the masonry arch to withstand, under uniform self-weight, is made apparent, showing that a loosening friction may hinder the overall structural bearing capacity of the masonry arch.

The present mechanical analysis may be generalized to other arch forms and contexts, likely by renouncing to possibly achieve manageable explicit analytical solutions, as sought and derived in the present investigation, and pushing on the conceived CP/MP numerical tool, which in principle may appropriately be generalized, to further explore the present basic, fundamental findings, in specific theoretical and practical masonry arch scenarios, in terms of structural bearing capacity prediction and assessment, as separately delivered, in the flourishing related literature on masonry arches, through different affine methodologies and techniques [14–32], including at finite friction [33–51], with mutually consistent results.

Acknowledgments

This work has been developed at the University of Bergamo, School of Engineering (Dalmine). The support by ministerial (MUR) funding "Fondi di Ricerca d'Ateneo ex 60%" at the University of Bergamo is gratefully acknowledged.
Editor and Reviewers are thanked, for the hints received at review stage, which have stimulated the outline of Discussion Section 3.3.

Compliance with Ethical Standards

The authors declare that they have no conflict of interest.

References

[1] Milankovitch, M. (1907). Theorie der Druckkurven, Zeitschrift für Mathematik und Physik, 55, pp. 1-27.

[2] Foce, F. (2007). Milankovitch's Theorie der Druckkurven: Good mechanics for masonry architecture, Nexus Network Journal, 9(2), pp. 185-210. DOI: 10.1007/s00004-007-0039-9.

[3] Heyman, J. (1969). The safety of masonry arches, International Journal of Mechanical Sciences, 11(4), pp. 363-385. DOI: 10.1016/0020-7403(69)90070-8.

[4] Heyman, J. (2009). La coupe des pierres, In: Proceedings of the 3rd International Congress on Construction History, Brandenburg University of Technology, Cottbus, Germany, 20–24 May 2009, 2, pp. 807–812.

[5] Cocchetti, G., Colasante, G., Rizzi, E. (2011). On the analysis of minimum thickness in circular masonry arches. Part I: State of the art and Heyman's solution. Part II: Present CCR solution. Part III: Milankovitch-type solution, Applied Mechanics Reviews, ASME, September 01, 2011, 64(5), Paper 050802 (Oct. 01, 2012), pp. 1-27. DOI: 10.1115/1.4007417.

[6] Rizzi, E., Rusconi, F., Cocchetti, G. (2014). Analytical and numerical DDA analysis on the collapse mode of circular masonry arches, Engineering Structures, 60(February 2014), pp. 241-257. DOI: 10.1016/j.engstruct.2013.12.023.

[7] Cocchetti, G., Rizzi, E. (2020). Analytical and numerical analysis on the collapse modes of least-thickness circular masonry arches at decreasing friction, Frattura ed Integrità Strutturale - Fracture and Structural Integrity, Special Issue on: Fracture and Damage Detection in Masonry Structures, 14(51), pp. 356-375, available Open Access at https://www.fracturae.com/index.php/fis/article/view/2554. DOI: 10.3221/IGF-ESIS.51.26.

[8] Cocchetti, G., Rizzi, E. (2020). Non-linear programming numerical formulation to acquire limit self-standing conditions of circular masonry arches accounting for limited friction, International Journal of Masonry Research and Innovation, Special Issue on: 10IMC Masonry Research in the Third Millennium From Theory to Practical Applications, 5(4), pp. 569-617. DOI: 10.1504/IJMRI.2020.111806.

[9] Cocchetti, G., Rizzi, E. (2020). Static upper/lower thrust and kinematic work balance stationarity for least-thickness circular masonry arch optimization, Journal of Optimization Theory and Applications, Special Issue on: Computational Optimization for Structural Engineering and Applications, 187(3), pp. 707-757, available Open Access at https://link.springer.com/article/10.1007/s10957-020-01772-0. DOI: 10.1007/s10957-020-01772-0.

[10] Cocchetti, G., Rizzi, E. (2021). Least-thickness symmetric circular masonry arch of maximum horizontal thrust, Archive of Applied Mechanics, 91(6), pp. 2617-2639, available Open Access at https://link.springer.com/article/10.1007/s00419-021-01909-1. DOI: 10.1007/s00419-021-01909-1.

[11] Cocchetti, G., Rizzi, E. (2024). Finite-friction least-thickness self-standing domains of symmetric circular masonry arches, Structures, Special Issue on Shells and Spatial Structures: Conceptual Design, Construction and Maintenance, Eds. Stefano Gabriele and Andrea Micheletti, Accepted 19 June 2024, Published online 8 July 2024, 66(August 2024), Paper 106800, pp. 1-20, available Open Access at https://www.sciencedirect.com/science/article/pii/S2352012424009524. DOI: 10.1016/j.istruc.2024.106800.

[12] Cocchetti, G., Rizzi, E. (2025). Finite-friction least-thickness self-standing domains of symmetric circular masonry arches. Part II: Milankovitch-like self-weight distribution, Structures, Accepted 25 March 2025, Published online 15 April 2025, 76(June 2025), Paper 108780, pp. 1-20, available Open Access at https://www.sciencedirect.com/science/article/pii/S2352012425005946. DOI: 10.1016/j.istruc.2025.108780.

[13] Cocchetti, G., Rizzi, E. (2025). Finite-friction least-thickness self-standing domains of symmetric circular masonry arches. Part III: Complementary representations, extremal conditions and collapse multiplicity, Structures, Accepted 28 July 2025, Available online 19 August 2025, 80(October 2025), Paper 109832, pp. 1-28, available Open Access at https://www.sciencedirect.com/science/article/pii/S2352012425016479. DOI: 10.1016/j.istruc.2025.109832.

[14] Kooharian, A. (1952). Limit analysis of voussoir (segmental) and concrete arches, Journal Proceedings of the American Concrete Institute, 49(12), pp. 317-328. DOI: 10.14359/11822.

[15] Livesley, R.K. (1978). Limit analysis of structures formed from rigid blocks, International Journal for Numerical and Analytical Methods in Engineering, 12(12), pp. 1853-1871. DOI: 10.1002/nme.1620121207.

[16] Livesley, R.K. (1992). A computational model for the limit analysis of three-dimensional masonry structures, Meccanica, 27(3), pp. 161-172. DOI: 10.1007/BF00430042.

[17] Como, M. (1992). Equilibrium and collapse of masonry bodies, Meccanica, 27(3), pp. 185-194. DOI: 10.1007/BF00430044.

[18] Boothby, T.E., Brown C.B. (1992). Stability of masonry piers and arches, Journal of Engineering Mechanics, ASCE, 118(2), pp. 367–383. DOI: 10.1061/(ASCE)0733-9399(1992)118:2(367).

[19] Boothby, T.E. (1996). Analytical approach to collapse mechanisms of circular masonry arch. Discussion on the paper by Blasi and Foraboschi (1994), with Closure by P. Foraboschi and C. Blasi, Journal of Structural Engineering, ASCE, 122(8), pp. 978-980. DOI: 10.1061/(ASCE)0733-9445(1996)122:8(978).

[20] Blasi, C., Foraboschi, P. (1994). Analytical approach to collapse mechanisms of circular masonry arch, Journal of Structural Engineering, ASCE, 120(8), pp. 2288-2309. DOI: 10.1061/(ASCE)0733-9445(1994)120:8(2288).

[21] Lucchesi, M., Padovani, C., Pasquinelli, G., Zani, N. (1997). On the collapse of masonry arches, Meccanica, 32(4), pp. 327-346. DOI: 10.1023/A:1004275223879.

[22] Ochsendorf, J.A. (2006). The masonry arch on spreading supports, The Structural Engineer, 84(2), pp. 29-36.

[23] Romano, A., Ochsendorf, J.A. (2009). The mechanics of Gothic masonry arches, International Journal of Architectural Heritage, 4(1), pp. 59–82. DOI: 10.1080/15583050902914660.

[24] Block, P., DeJong, M., Ochsendorf, J. (2006). As hangs the flexible line: equilibrium of masonry arches, Nexus Network Journal, 8(2), pp. 13-24. DOI: 10.1007/s00004-006-0015-9.

[25] Alexakis, H., Makris, N. (2013). Minimum thickness of elliptical masonry arches, Acta Mechanica, 224(12), pp. 2977-2991. DOI: 10.1007/s00707-013-0906-2.

[26] Alexakis, H., Makris, N. (2014). Limit equilibrium analysis and the minimum thickness of circular masonry arches to withstand lateral inertial loading, Archive of Applied Mechanics, 84(5), pp. 757-772. DOI: 10.1007/s00419-014-0831-4.

[27] Alexakis, H., Makris, N. (2015). Limit equilibrium analysis of masonry arches, Archive of Applied Mechanics, 85(9-10), pp. 1363-1381. DOI: 10.1007/s00419-014-0963-6.

[28] Makris, N., Alexakis, H. (2013). The effect of stereotomy on the shape of the thrust-line and the minimum thickness of semicircular masonry arches, Archive of Applied Mechanics, 83(10), pp. 1511-1533. DOI: 10.1007/s00419-013-0763-4.

[29] Nikolić, D. (2017). Thrust line analysis and the minimum thickness of pointed masonry arches, Acta Mechanica, 228(6), pp. 2219-2236. DOI: 10.1007/s00707-017-1823-6.

[30] Gáspár, O., Sipos, A.A., Sajtos, I. (2018). Effect of stereotomy on the lower bound value of minimum thickness of semi-circular masonry arches, International Journal of Architectural Heritage, 12(6), pp. 899-921. DOI: 10.1080/15583058.2017.1422572.

[31] Gáspár, O., Sajtos, I., Sipos, A.A. (2022). Multi-hinge failure mechanisms of masonry arches subject to self-weight as derived from minimum thickness analysis, International Journal of Architectural Heritage, 17(12), pp. 1921-1949. DOI: 10.1080/15583058.2022.2084702.

[32] Nodargi, N.A., Bisegna, P. (2020). Thrust line analysis revisited and applied to optimization of masonry arches, International Journal of Mechanical Sciences, 179(1 August 2020), 105690179, pp. 1-13. DOI: 10.1016/j.ijmecsci.2020.105690.

[33] Drucker, D.C. (1954). Coulomb friction, plasticity, and limit loads, Journal of Applied Mechanics, 21(1), pp. 71-74. DOI: 10.1115/1.4010821.

[34] Boothby, T.E. (1994). Stability of masonry piers and arches including sliding, Journal of Engineering Mechanics, ASCE, 120(2), pp. 304-319. DOI: 10.1061/(ASCE)0733-9399(1994)120:2(304).

[35] Sinopoli, A., Corradi, M., Foce, F. (1997). Modern formulation for preelastic theories on masonry arches, Journal of Engineering Mechanics, ASCE, 123(3), pp. 204-213. DOI: 10.1061/(ASCE)0733-9399(1997)123:3(204).

[36] Sinopoli, A., Aita, D., Foce, F. (2007). Further remarks on the collapse mode of masonry arches with Coulomb friction, Proceedings of 5th International Conference on Arch Bridges (ARCH'07), Funchal, Madeira, Portugal, September 12-14, 2007, P.B. Lourenço, D.B. Oliveira, A. Portela (Eds.), Multicomp, Lda Publishers, Madeira, pp. 649-657.

[37] Baggio, C., Trovalusci, P. (2000). Collapse behaviour of three-dimensional brick-block systems using non-linear programming, Structural Engineering and Mechanics, 10(2), pp. 181-195. DOI: 10.12989/sem.2000.10.2.181.

[38] Rios, A.J., Nela, B., Pingaro, M., Reccia, E., Trovalusci, P. (2025). Parametric analysis of masonry arches following a limit analysis approach: Influence of joint friction, pier texture, and arch shallowness, Mathematics and Mechanics of Solids, OnlineFirst 11 July 2023, 30(1), pp. 137-165. DOI: 10.1177/10812865231175385.

[39] Casapulla, C., Lauro, F. (2000). A simple computation tool for the limit-state analysis of masonry arches, Proceedings of 5th International Congress on Restoration of Architectural Heritage, Università di Firenze, 17-24 September 2000, CDROM Proc., pp. 2056-2064.

[40] Gilbert, M., Casapulla, C., Ahmed, H.M. (2006). Limit analysis of masonry block structures with non-associative frictional joints using linear programming, Computers and Structures, 84(13-14), pp. 873-887. DOI: 10.1016/j.compstruc.2006.02.005.

[41] Smars, P. (2010). Kinematic stability of masonry arches, Advanced Materials Research, 133-134, pp. 429-434. DOI: 10.4028/www.scientific.net/AMR.133-134.429.

[42] D'Ayala, D., Tomasoni, E. (2011). Three-dimensional analysis of masonry vaults using limit state analysis with finite friction, International Journal of Architectural Heritage, 5(2), pp. 140-171. DOI: 10.1080/15583050903367595.

[43] Trentadue, F., Quaranta, G. (2013). Limit analysis of frictional block assemblies by means of fictitious associative-type contact interface laws, International Journal of Mechanical Sciences, 70(May 2013), pp. 140-145. DOI: 10.1016/j.ijmecsci.2013.02.012.

[44] Trentadue, F., De Tommasi, D., Marasciuolo, N., Vitucci, G. (2024). Thrust in a symmetric masonry arch with frictional joints on spreading supports, Acta Mechanica, 235(2), pp. 659-670. DOI: 10.1007/s00707-023-03759-0.

[45] Trentadue, F., De Tommasi, D., Marasciuolo, N. (2025). A new approach to the limit analysis of masonry structures as assemblies of rigid-plastic blocks with frictional sliding contacts, Structures, 76(June 2025), 108895, pp. 1-7. DOI: 10.1016/j.istruc.2025.108895.

[46] Bagi, K. (2014). When Heyman's Safe Theorem of rigid block systems fails: Non-Heymanian collapse modes of masonry structures, International Journal of Solids and Structures, 51(14), pp. 2696-2705. DOI: 10.1016/j.ijsolstr.2014.03.041.

[47] Aita, D., Barsotti, R., Bennati, S. (2019). Looking at the collapse modes of circular and pointed masonry arches through the lens of Durand-Claye's stability area method, Archive of Applied Mechanics, 89(8), pp. 1537-1554. DOI: 10.1007/s00419-019-01526-z.

[48] Aita, D., Barsotti, R., Bennati, S. (2021). Arch-piers systems subjected to vertical loads: a comprehensive review of rotational, sliding and mixed collapse modes, Archive of Applied Mechanics, 91(1), pp. 241-256. DOI: 10.1007/s00419-020-01766-4.

[49] Aita, D., Bruggi, M., Garavaglia, E. (2024). Collapse analysis of masonry arches and domes considering finite friction and uncertainties in compressive strength, Engineering Failure Analysis, 163(Part A, September 2024), 108462, pp. 1-20. DOI: 10.1016/j.engfailanal.2024.108462.

[50] Gáspár, O., Sajtos, I., Sipos, A.A. (2021). Friction as a geometric constraint on stereotomy in the minimum thickness analysis of circular and elliptical masonry arches, International Journal of Solids and Structures, 225(15 August 2021), 111056, pp. 1-18. DOI: 10.1016/j.ijsolstr.2021.111056.

[51] Hua, Y., Milani, G. (2022). Rigid Block Limit Analysis of Masonry Arches with Associated and Non-associated Slides, in: G. Milani and V. Sarhosis (Eds.), From Corbel Arches to Double Curvature Vaults, Springer Nature Switzerland AG, pp. 169-203. DOI: 10.1007/978-3-031-12873-8_7.

Tables and Figures

α	$A = \alpha \cot(\alpha/2)$	$\mu = \tan\varphi$	φ
50°	0.87266462599716480	1.87143532973480	0.09000903476256731	5.14°
60°	1.04719755119659800	1.81379936423421800	0.14469706660443300	8.23°
70°	1.22173047639603100	1.74481194464108500	0.21345737738930700	12.05°
80°	1.39626340159546400	1.66400192505920600	0.29662343852846610	16.52°
90°	1.57079632679489700	1.57079632679489700	0.39526525214044650	21.57°
100°	1.74532925199433000	1.46450513163136000	0.51170486727066820	27.10°
110°	1.91986217719376300	1.34430196879477800	0.65018047046113610	33.03°
120°	2.09439510239319500	1.20919957615614500	0.81794121892822150	39.28°
130°	2.26892802759262800	1.05801851506895900	1.02738465345878700	45.77°
139.23°	2.43006910376934900	0.90294523971796420	1.27702136343519800	51.94°

η	h	$\hat{h} = \eta h$	β_r		β_s	
0.01129405156554886	0.87704007573899140	0.00990533584044904	0.58623340347298100	33.59°	-	-
0.02284890993937951	0.82505176065062910	0.01885153337443272	0.68871799568290660	39.46°	-	-
0.04126132618229432	0.76488657994147880	0.03156023466742490	0.78417324842073000	44.93°	-	-
0.06865046333037354	0.69680832880605750	0.04783621462499120	0.87188055317138810	49.96°	-	-
0.10747803810747630	0.62088120617187200	0.06673109393715631	0.95092473646450030	54.48°	-	-
0.16073564997765250	0.53690161310298930	0.08629922975615907	1.01981202565138600	58.43°	-	-
0.23229481316167410	0.44433415621380250	0.10321651979903540	1.07569350808646700	61.63°	-	-
0.32760650771104190	0.34226280485733750	0.11212752221869820	1.11247606511672500	63.74°	-	-
0.45544960764410850	0.22942387215034140	0.10449101255506510	1.11490736041812900	63.88°	-	-
0.61831824410743234	0.11476008247974080	0.07095825234441760	1.04255680859359900	59.73°	0.31873218530450270	18.26°

Table 1: Numerical data for below-left Triple point T α values, lower *ss* activation boundary.

α	$A = \alpha \cot(\alpha/2)$	$\mu = \tan\varphi$	φ
50°	0.87266462599716480	1.87143532973480600	0.05497570346510800	3.15°
60°	1.04719755119659800	1.81379936423421800	0.09437585193695087	5.39°
70°	1.22173047639603100	1.74481194464108500	0.14852850329071720	8.45°
80°	1.39626340159546400	1.66400192505920600	0.21939417869493800	12.37°
90°	1.57079632679489700	1.57079632679489700	0.30921544433022860	17.18°
100°	1.74532925199433000	1.46450513163136000	0.42126739930528230	22.84°
110°	1.91986217719376300	1.34430196879477800	0.56114231328526210	29.30°
120°	2.09439510239319500	1.20919957615614500	0.73904014399885410	36.47°
130°	2.26892802759262800	1.05801851506895900	0.97446051271672300	44.26°
139.23°	2.43006910376934900	0.90294523971796420	1.27702136343519800	51.94°

η	h	$\hat{h} = \eta h$	β_r	β_s
0.02473756757010358	0.81796051158059980	0.02023435342490158	0.70106771543102900	40.17°	0.38587706990102850	22.11°
0.04893473026113250	0.74396717568949410	0.03640583306550197	0.81310317866461310	46.59°	0.43644016449691190	25.01°
0.08540225129103124	0.66191861685817520	0.05652934005113371	0.91037784650140520	52.16°	0.47305640415782920	27.10°
0.13536969689479030	0.57476585419568900	0.07780587946794567	0.99097505670022910	56.78°	0.49437846539507460	28.33°
0.19861020902254290	0.48571448414217490	0.09646785522075397	1.05325733970550000	60.35°	0.49979588237267000	28.64°
0.27340592475991990	0.39794220854945500	0.10879975752946870	1.09583052138397800	62.79°	0.48947339785144310	28.04°
0.35688276939974800	0.31434224079882500	0.11218332940560710	1.11739343750990710	64.02°	0.46425337526871950	26.60°
0.44557248508706980	0.23736317106905980	0.10576249800138820	1.11645746516472900	63.97°	0.42546668035123510	24.38°
0.53598706555619140	0.16896586825104440	0.09056351990300989	1.09091355491837300	62.50°	0.37472176827239250	21.47°
0.61831824107432340	0.11476008247974080	0.07095825234441760	1.04255680859359900	59.73°	0.31873218530450270	18.26°

Table 2: Numerical data for below-left Triple point T α values, upper *is* activation boundary.

Table 3: Numerical data for above-right Triple point T α values, lower is activation boundary.

α		$A = \alpha \cot(\alpha/2)$	$\mu = \tan\varphi$	φ
139.23°	2.430069103769349	0.9029452397179642	1.277021363435198	51.94°
140°	2.443460952792061	0.8893470554080446	1.354481816772004	53.56°
141°	2.460914245312005	0.8714554396703472	1.473086517212808	55.83°
142°	2.478367537831948	0.8533703791562588	1.618926266229822	58.30°
143°	2.495820830351891	0.8350899681515206	1.804714632107875	61.01°
144°	2.513274122871835	0.8166122645535406	2.053340082340885	64.03°
145°	2.530727415391778	0.7979352890558678	2.411307943775690	67.48°
145.03°	2.531269027051532	0.7973524943847578	2.425074829552999	67.59°
145.19°	2.534077907926731	0.7943269204166809	2.499872740239247	68.20°
146°	2.548180707911721	0.7790570243096621	2.992559342922343	71.52°
147°	2.565634000431664	0.7599754140614066	4.188503928025442	76.57°
148°	2.583087292951608	0.7406883622660837	9.392171216495615	83.92°
148.44°	2.590843443008955	0.7320508075688773	∞	90°

η	h	$\hat{h} = \eta h$	β_r		β_s	
0.6183182410743234	0.1147600824797408	0.07095825234441760	1.042556808593599	59.73°	0.3187321853045027	18.26°
0.6348673020101641	0.1048004938854927	0.06653440680241548	1.029325458000376	58.98°	0.3062961807905047	17.55°
0.6574380548990384	0.09174301620103466	0.06031535012177919	1.009039703392926	57.81°	0.2886628399696978	16.54°
0.6813141909731173	0.07861416267212113	0.05356094463998524	0.9844547672019693	56.41°	0.2691356091257387	15.42°
0.7067487077395226	0.06544003721216479	0.04624966173412373	0.9542262796217054	54.67°	0.2473007050977317	14.17°
0.7341129938258968	0.05226188132632393	0.03836612616344139	0.9162454238036576	52.50°	0.2225546608960530	12.75°
0.7639951159151049	0.03914906299459148	0.02990969292052066	0.8669014040119687	49.67°	0.1939495136916744	11.11°
0.7649721138056281	0.03874434109562339	0.02963834050592528	0.8651268297141475	49.57°	0.1929850178865950	11.06°
0.7700943048247798	0.03664842932766100	0.02822274670600517	0.8556381572288650	49.02°	0.1878971047022184	10.77°
0.7974372760995779	0.02623071924405118	0.02091735330410895	0.7991320240763997	45.79°	0.1598207389921312	9.16°
0.8366728854899335	0.01379482210355162	0.01154175361419885	0.6955335779968959	39.85°	0.1166384370037724	6.68°
0.8890121355419089	0.002815462172869775	0.002502980038840421	0.4812527115647549	27.57°	0.05298618070424508	3.04°
0.9282032302755092	0	0	0	0°	0	0°

Table 4: Numerical data for above-right Triple point T α values, upper ss activation boundary.

α		$A = \alpha\cot(\alpha/2)$	$\mu = \tan\varphi$	φ
139.23°	2.430069103769349	0.9029452397179642	1.277021363435198	51.94°
140°	2.443460952792061	0.8893470554080446	1.307632471913603	52.59°
141°	2.460914245312005	0.8714554396703472	1.349135415012182	53.45°
142°	2.478367537831948	0.8533703791562588	1.392589247391815	54.32°
143°	2.495820830351891	0.8350899681515206	1.438150443539977	55.19°
144°	2.513274122871835	0.8166122645535406	1.485992916770067	56.06°
145°	2.530727415391778	0.7979352890558678	1.536310506737699	56.94°
145.03°	2.531269027051532	0.7973524943847578	1.537913842804308	56.97°
145.19°	2.534077907926731	0.7943269204166809	1.546270800988722	57.11°
146°	2.548180707911721	0.7790570243096621	1.589319905991465	57.82°
147°	2.565634000431664	0.7599754140614066	1.645264118687524	58.71°
148°	2.583087292951608	0.7406883622660837	1.704416567879248	59.60°
148.44°	2.590843443008955	0.7320508075688773	1.731812568397235	60.00°

η	h	$\hat{h} = \eta h$	β_r		β_s	
0.6183182410743234	0.1147600824797408	0.07095825234441760	1.042556808593599	59.73°	0.3187321853045027	18.26°
0.6423765869948384	0.1106739394418327	0.07109434748791791	1.009801874322984	57.86°	0.3137279371848453	17.98°
0.6762319048530182	0.1054486016205901	0.07130770873797874	0.9575854454008237	54.87°	0.3071305814093611	17.60°
0.7136534950998119	0.1003374375268112	0.07160616298036785	0.8896459827234634	50.97°	0.3004493903428071	17.21°
0.7559715501604206	0.09534147139418983	0.07207543992444109	0.7955027541630808	45.58°	0.2936860146935511	16.83°
0.8058695603547605	0.09046170913761230	0.07290033777166784	0.6479743066207576	37.13°	0.2868420964877965	16.43°
0.8709718871303817	0.08569913963617554	0.07464154137436991	0.3034435654243437	17.39°	0.2799192689005079	16.04°
0.8734660698200911	0.08555323265580011	0.07472784588826560	0.2797031945436853	16.03°	0.2797031945436853	16.03°
0.8872221963291937	0.08479836323759743	0.07523499007678195	0	0°	0.2785814079040845	15.96°
0.9652117392505392	0.08105473601353599	0.07823498272211839	0	0°	0.2729191561311004	15.64°
1.078728360839722	0.07652945691530436	0.08255449561420038	0	0°	0.2658433733226257	15.23°
1.220187429685936	0.07212424778334321	0.08800510052078909	0	0°	0.2586935265232397	14.82°
1.296796328257749	0.07020537620120067	0.09104207408167096	0	0°	0.2554928205520628	14.64°

Table 5: Numerical data for among-asymptotes α values, with Overturning appearance.

α		$A = \alpha \cot(\alpha/2)$	$\mu = \tan\varphi$	φ
148.44°	2.590843443008955	0.7320508075688773	∞ | 1.731812568397235	90° | 60.00°
149°	2.600540585471551	0.7211937321750033	∞ | 1.767085997834371	90° | 60.49°
150°	2.617993877991494	0.7014893453974441	∞ | 1.833622356885605	90° | 61.39°
150.29°	2.623074865083552	0.6957132834961226	∞ | 1.853774888450581	90° | 61.66°
151°	2.635447170511438	0.6815729809352341	∞ | 2.692804304651327	90° | 69.63°
151.74°	2.648388899151005	$0.\bar{6}$	∞ | ∞	90° | 90°

η	h	$\hat{h} = \eta h$	β_r		β_s	
0.9282032302755092	0	0	0	0°	0	0°
1.007982485874711	0	0	0	0°	0	0°
1.184327905492372	0	0	0	0°	0	0°
1.247668494544594	0	0	0	0°	0	0°
1.444926206694904	0	0	0	0°	0	0°
2	0	0	0	0°	0	0°

η	h	$\hat{h} = \eta h$	β_r		β_s	
1.296796328257749	0.07020537620120067	0.09104207408167096	0	0°	0.2554928205520628	14.64°
1.411572435444959	0.06784004212696152	0.09576113348584367	0	0°	0.2514712126887959	14.41°
1.743429298237447	0.06367776279113474	0.1110176772962786	0	0°	0.2441780197254673	13.99°
2	0.06248908922171235	0.1249781784434247	0	0°	0.242041738032830	13.87°
2	0.03194950932453210	0.06389901864906419	0	0°	0.1758656822079104	10.08°
2	0	0	0	0°	0	0°

arch state	η	μ	$\varphi = \operatorname{atan}\mu$	α	β_r	β_s
SAFE	0.5	1.0	45°	130°	-	-
SR	0.5	1.0	45°	130.09°	63.27°	-
	0.5	0.99699	44.91°	130°	63.27°	-
	0.49539	1.0	45°	130°	63.35°	-

Table 6: Characteristic data of arch instances with reference state $\eta = 0.5$, $\mu = 1.0$ ($\varphi = 45°$) leading to mixed SR collapse for $\alpha \simeq 130°$. Arch illustrations in Fig. 16; further values in itemized text.

arch state	η	μ	$\varphi = \operatorname{atan}\mu$	α	β_r	β_s
SAFE	0.8	1.8	$\simeq 61°$	144°	-	-
RS	0.8	1.8	$\simeq 61°$	144.74°	41.21°	14.20°
	0.8	1.9364	62.69°	145°	42.07°	13.39°
	0.81705	1.8	$\simeq 61°$	145°	37.81°	14.20°

Table 7: Characteristic data of arch instances with reference state $\eta = 0.8$, $\mu = 1.8$ ($\varphi \simeq 61°$) leading to mixed RS collapse for $\alpha \simeq 145°$. Arch illustrations in Fig. 17; further values in itemized text.

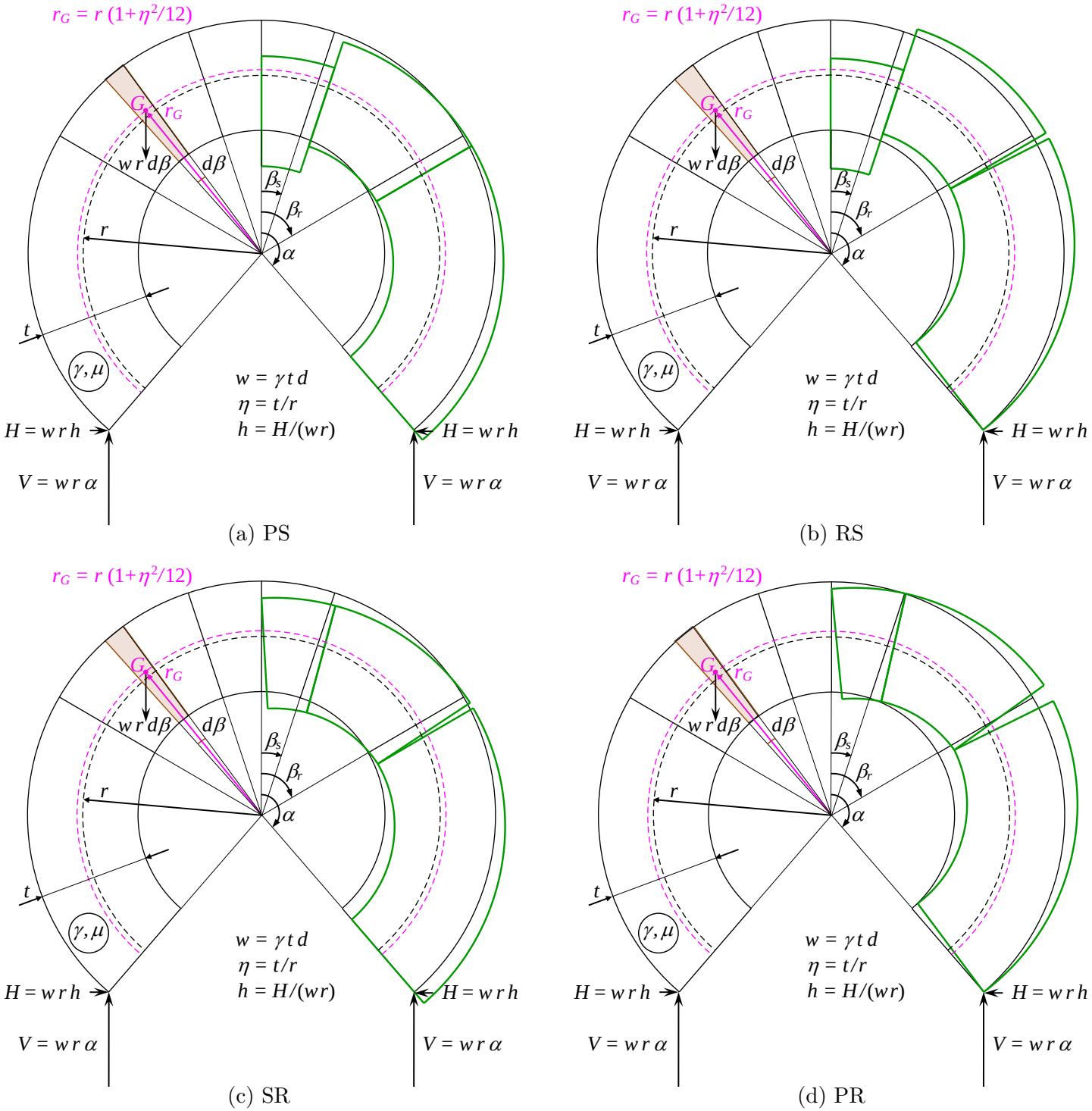

Figure 1: Analytical sketches of a possibly self-standing/collapsing symmetric circular continuous masonry arch with inner radius r, thickness t (thickness-to-radius ratio $\eta = t/r$), out-of-plane depth d, uniform specific weights per unit volume γ and per unit length of geometrical centreline of the arch $w = \gamma t d$, and inherent friction coefficient μ, with indication of the various characteristic variables (horizontal shoulder reaction H opposite of horizontal thrust H, and non-dimensional horizontal thrust $h = H/(wr)$, vertical shoulder reaction V opposite of half-arch weight $W = wr\alpha$; half-angle of embrace α, sliding β_s and rotational β_r angular inner-joint positions from the crown). The plots specifically refer to the arch features for the overcomplete case of landmark "Triple point T", displaying concomitant multiple (four) underlying (symmetric) collapse modes, represented, for the half-arch, on the right of the crown: (a) Purely-Sliding (PS); (b) mixed Rotational-Sliding (RS); (c) mixed Sliding-Rotational (SR); (d) Purely-Rotational (PR). After Triple point T, rotational components may become Overturning ($\beta_r = 0$), as Overturning-Sliding (OS) at finite friction or Purely-Overturning (PO) at infinite friction. On the left of the crown, infinitesimal arch elements with real centroid G, for true Milankovitch-like uniform self-weight distribution at larger radial distance $r_G = r(1 + \eta^2/12)$, versus classical approximate Heyman-like uniform self-weight distribution at radial distance r, are depicted.

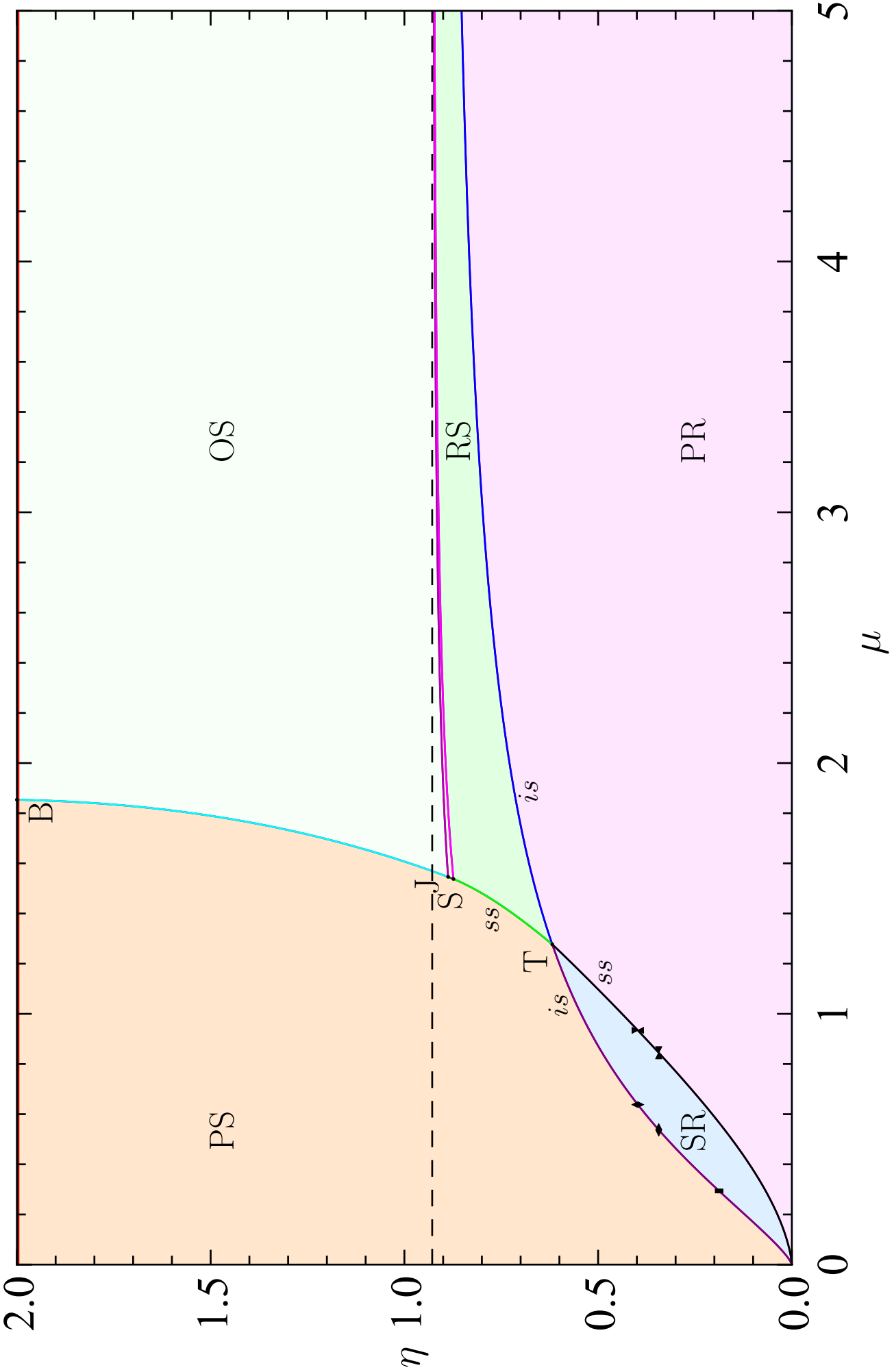

Figure 2: Analytical η-μ plot with domains of arch states.

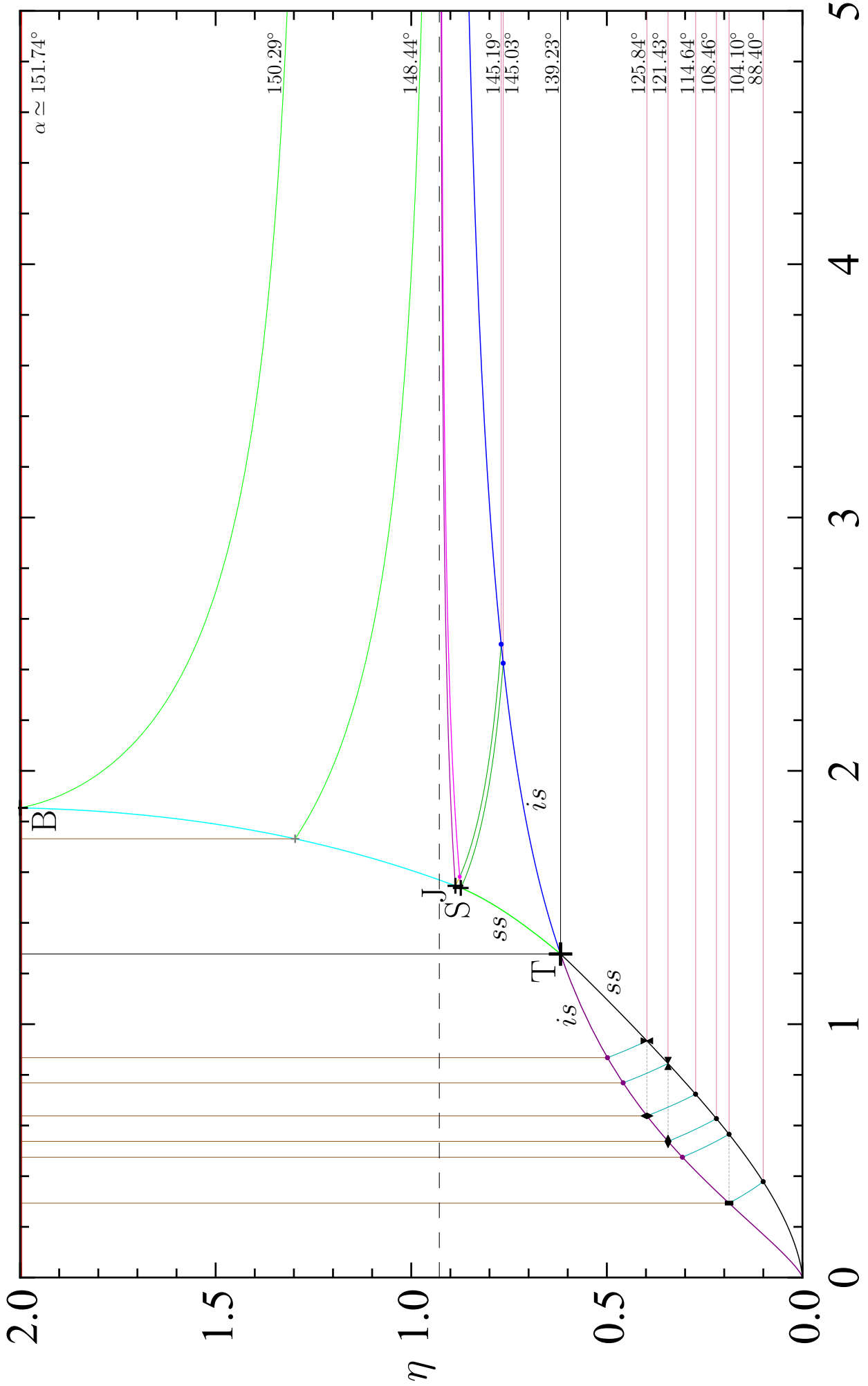

Figure 3: Analytical η-μ plot with landmark α states.

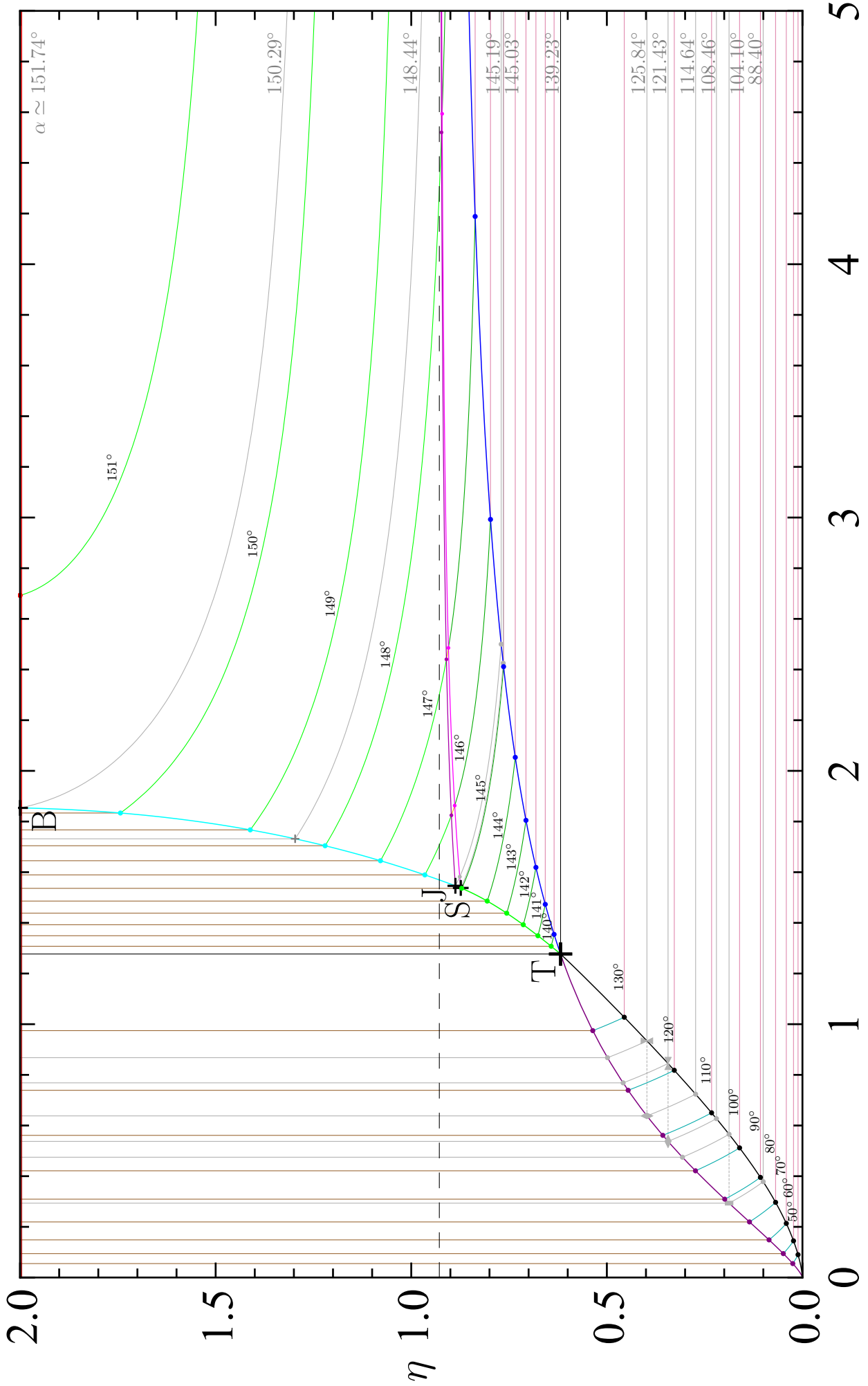

Figure 4: Analytical η-μ plot with landmark and sampled α states.

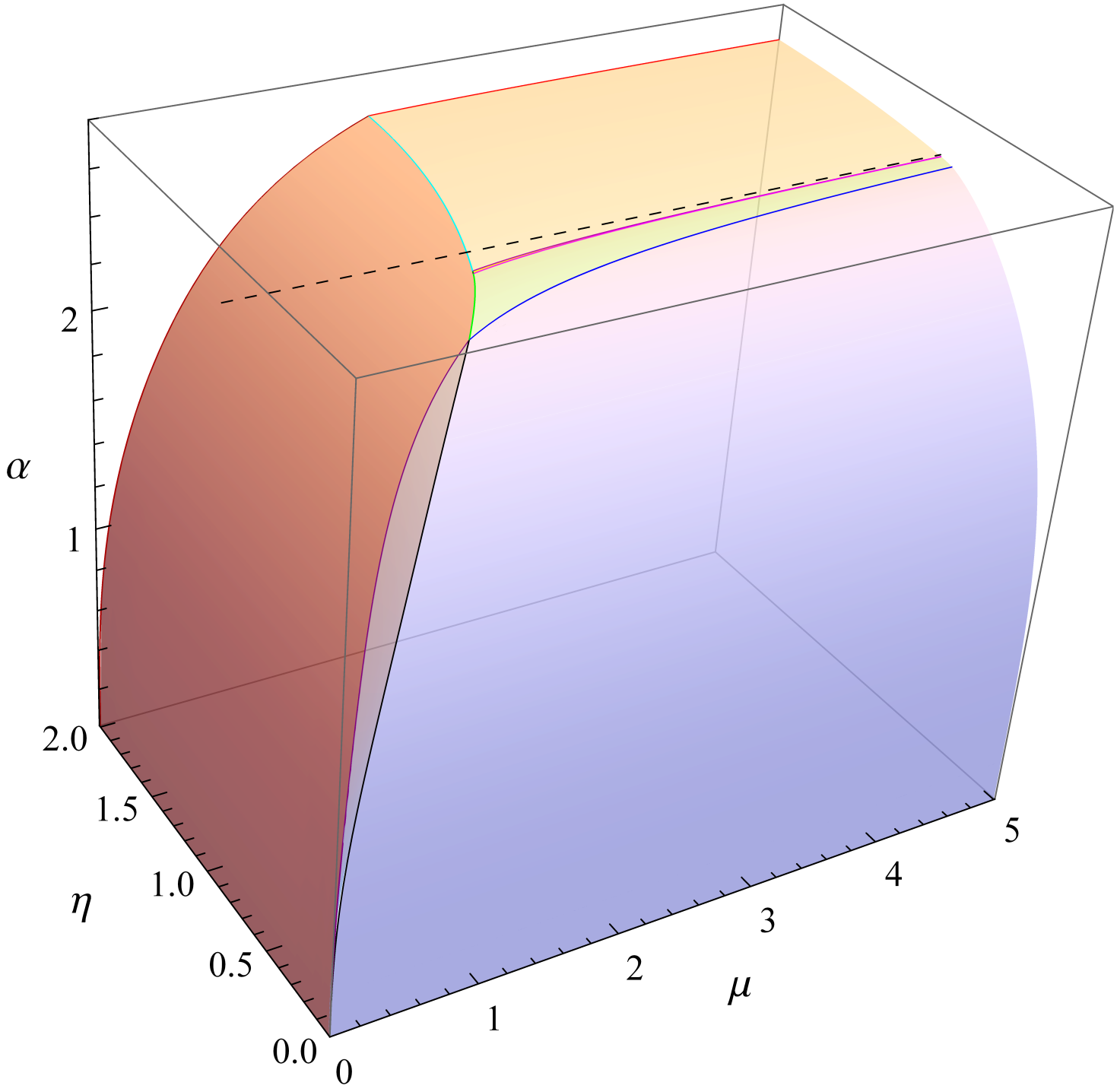

Figure 5: Three-dimensional surface representation of (η; μ, α) safe (inner volume) vs. collapse (wrapping surface) arch states.

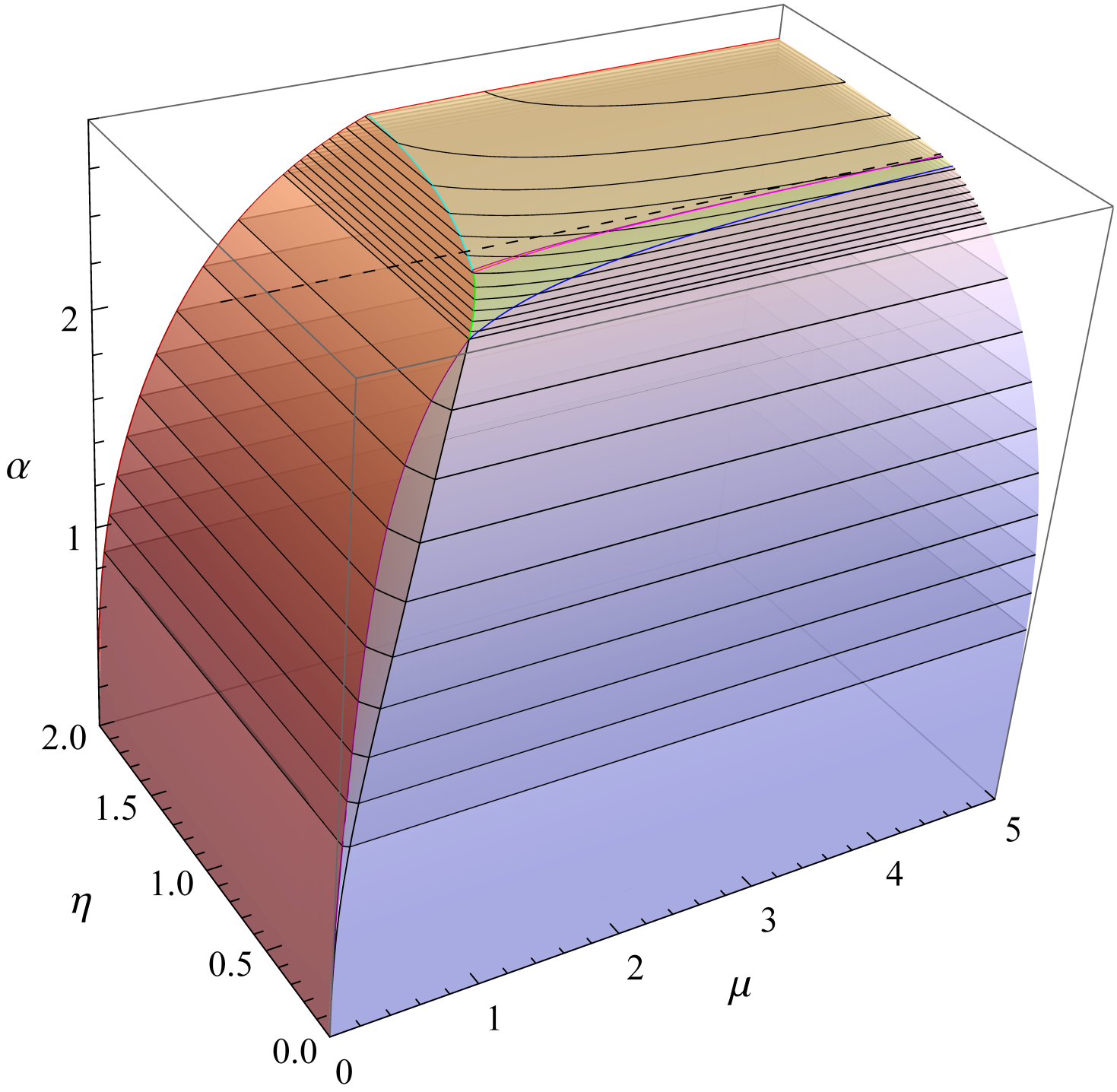

Figure 6: Three-dimensional surface representation of (η; μ, α) safe (inner volume) vs. collapse (wrapping surface) arch states, with sampled iso-α contour lines and planes.

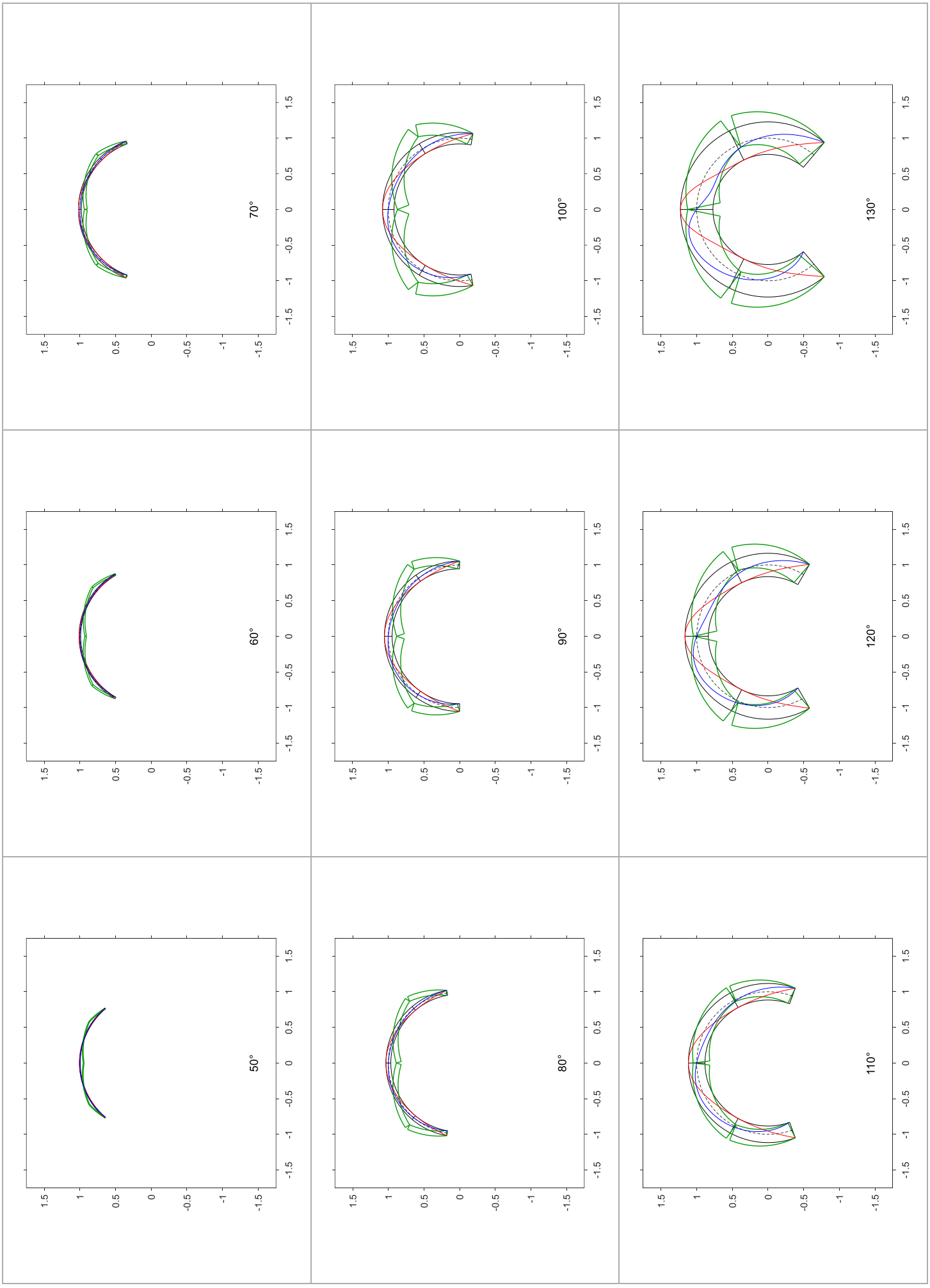

Figure 7: Frame of arch states at sampled below-left Triple point T α values; PR modes.

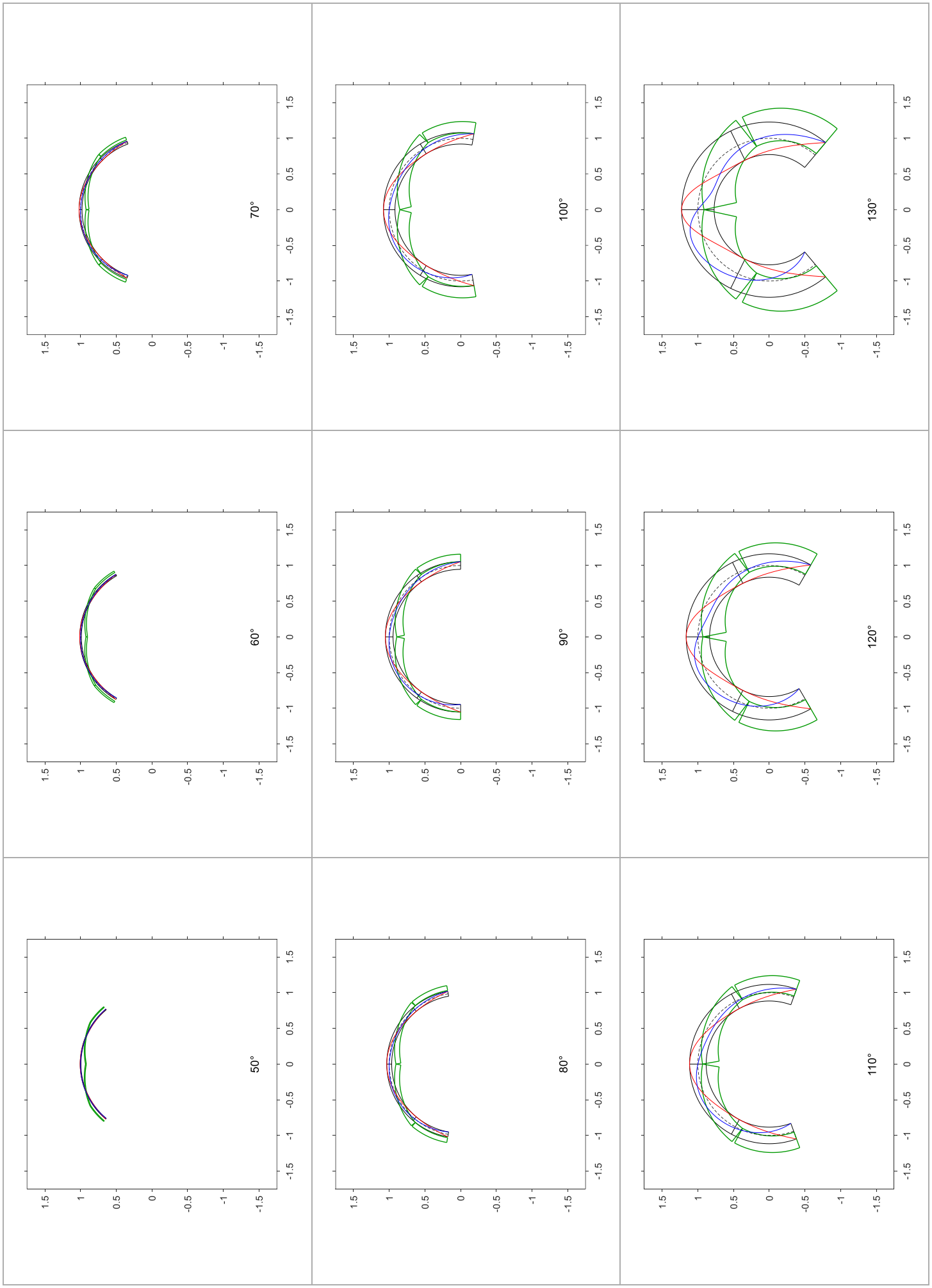

Figure 8: Frame of arch states at sampled below-left Triple point T α values; lower SR modes.

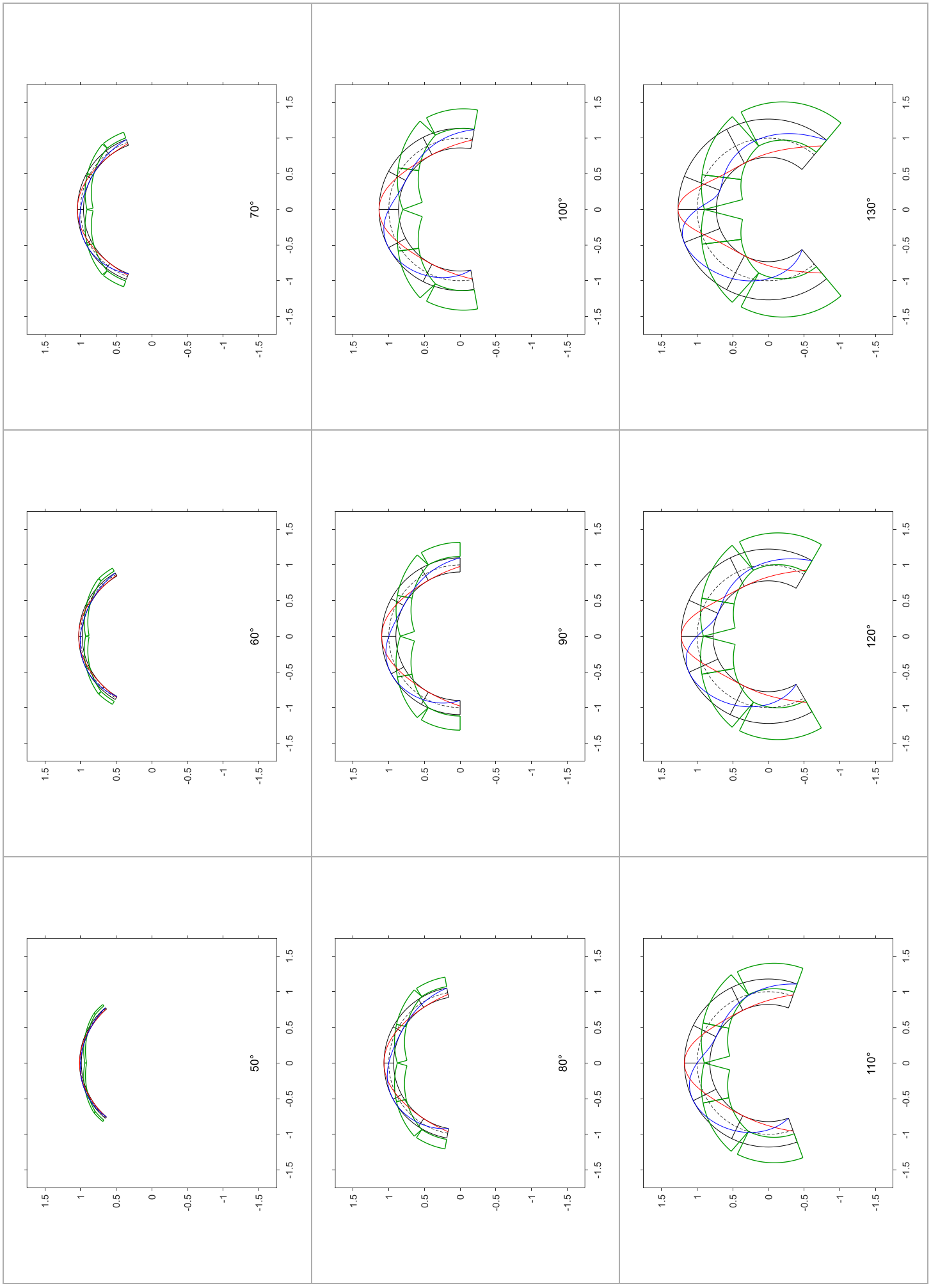

Figure 9: Frame of arch states at sampled below-left Triple point T α values; upper SR modes.

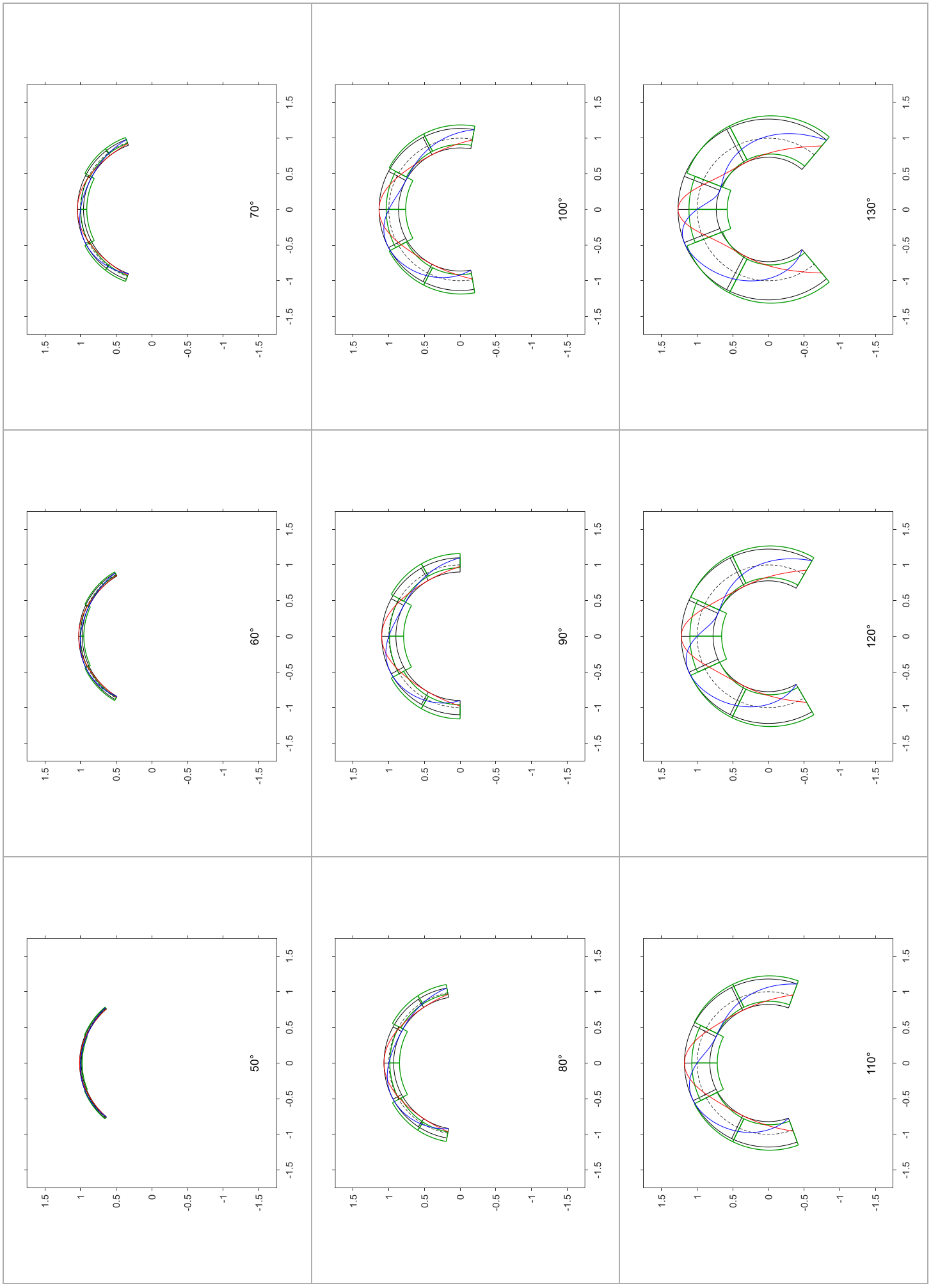

Figure 10: Frame of arch states at sampled below-left Triple point T α values; PS modes.

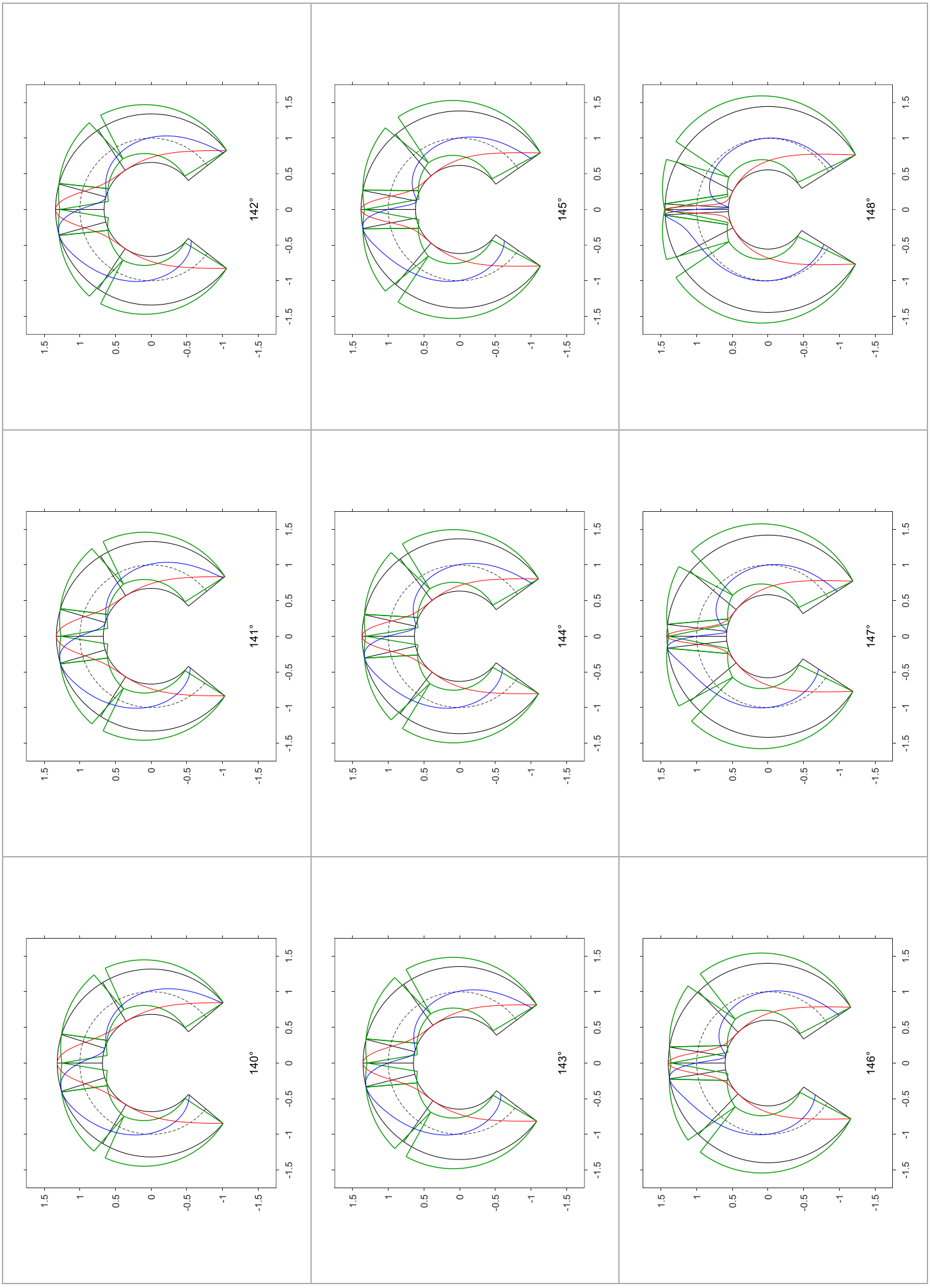

Figure 11: Frame of arch states at sampled above-right Triple point T α values; PR modes.

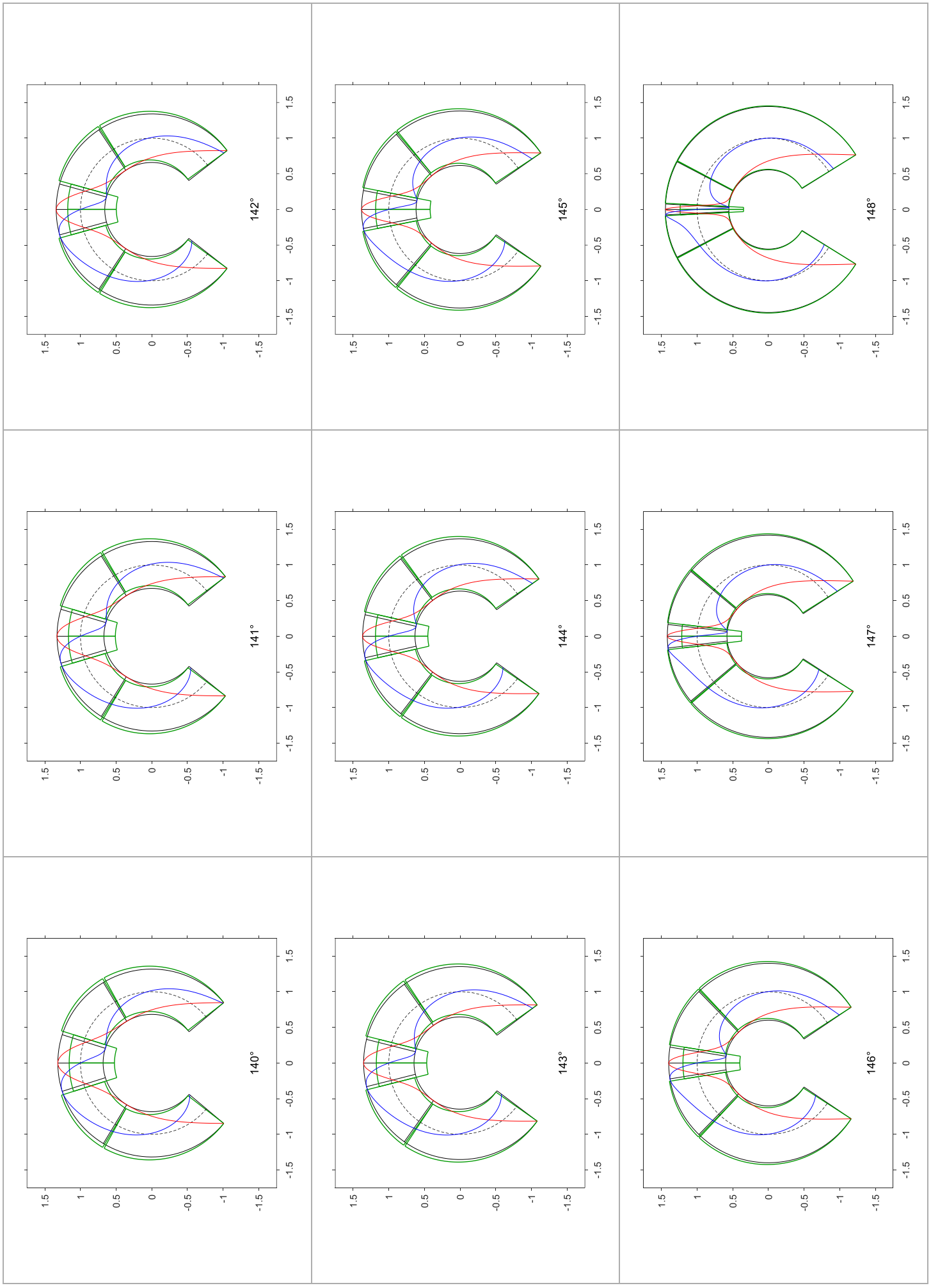

Figure 12: Frame of arch states at sampled above-right Triple point T α values; lower RS modes.

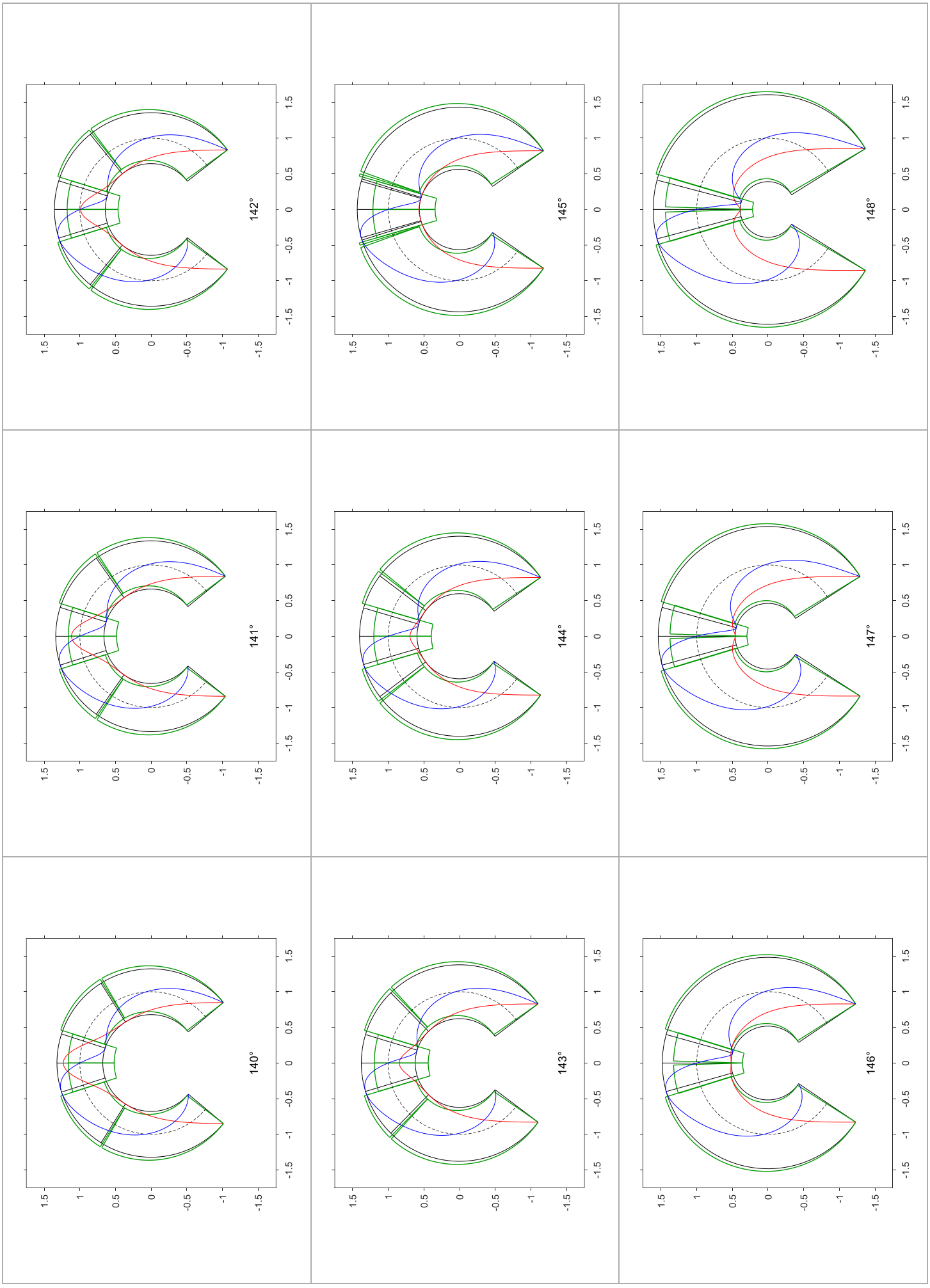

Figure 13: Frame of arch states at sampled above-right Triple point T α values; upper RS modes.

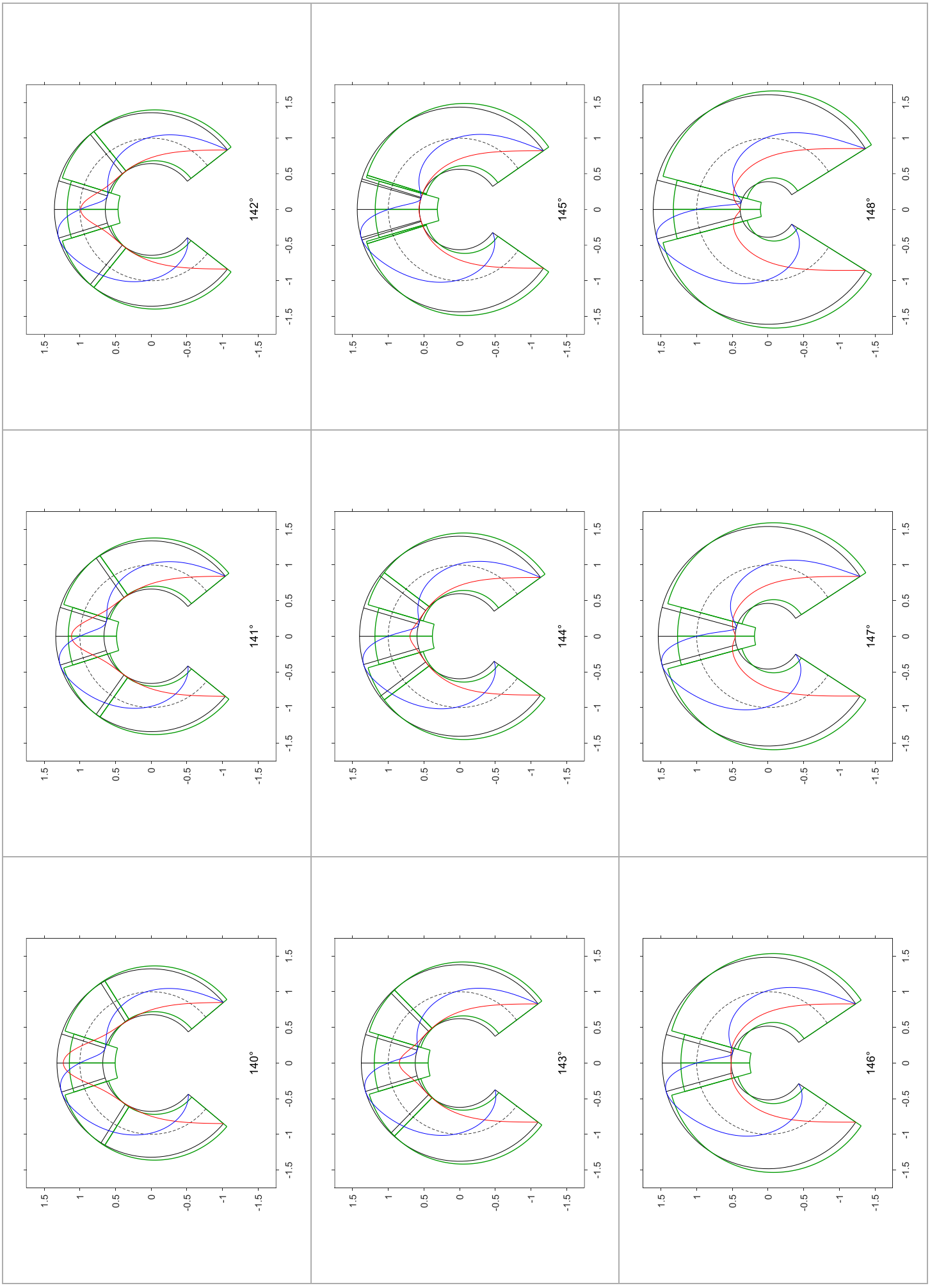

Figure 14: Frame of arch states at sampled above-right Triple point T α values; PS modes.

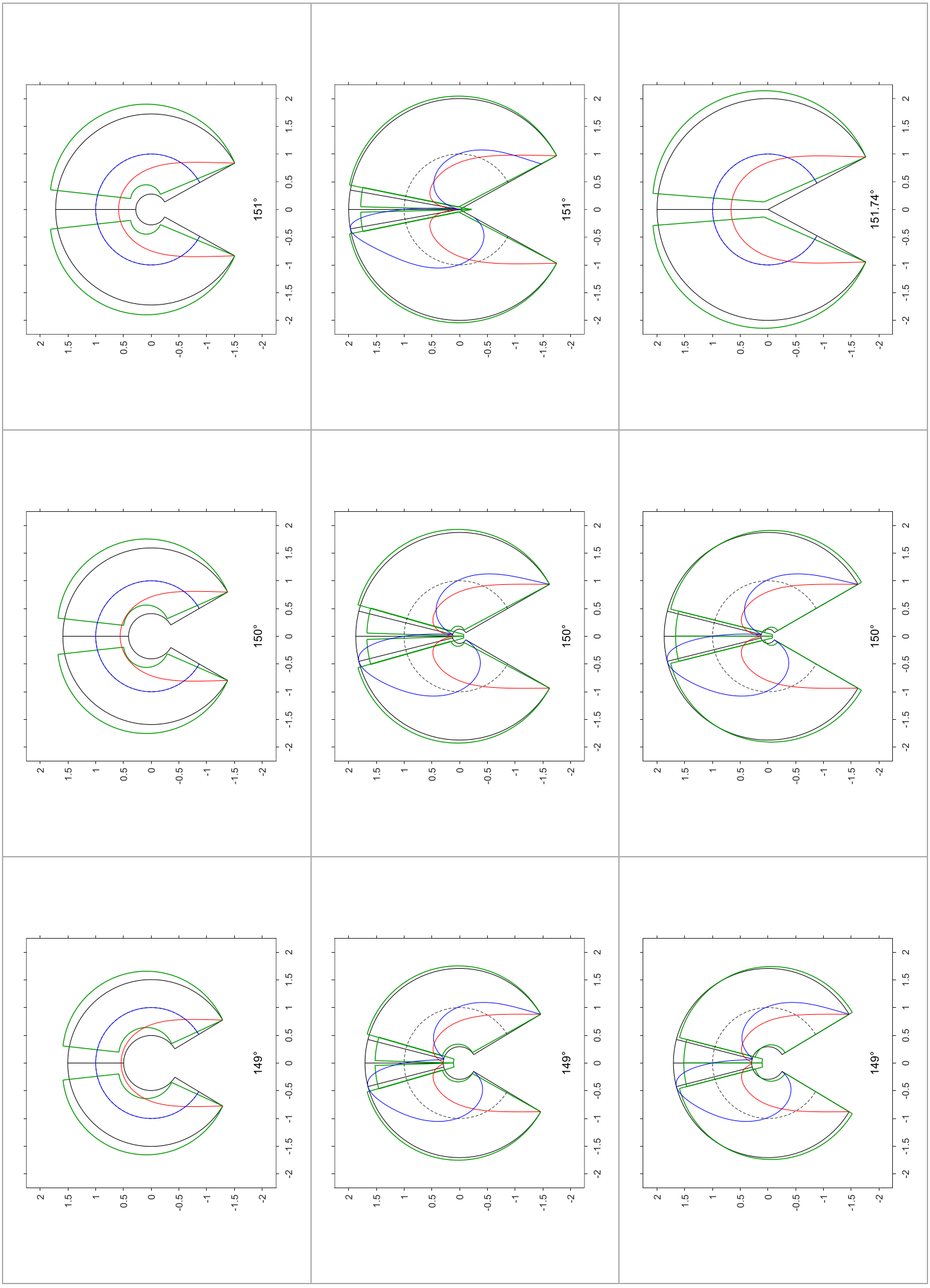

Figure 15: Frame of arch states at sampled among-asymptotes α values; PO, OS and PS modes.

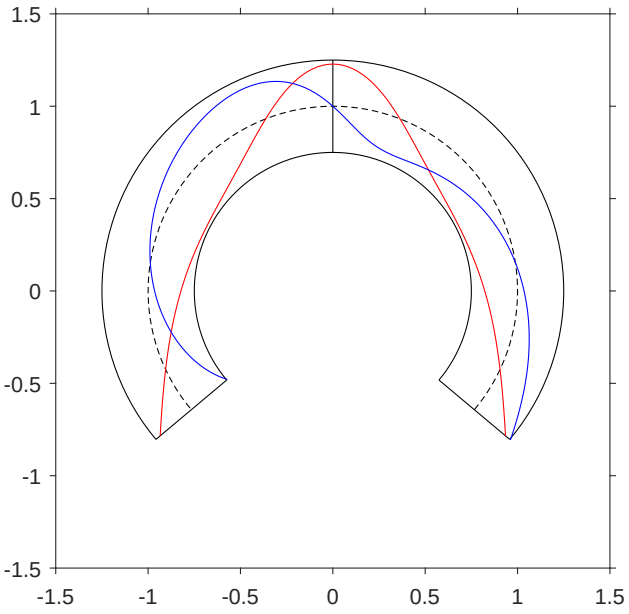

(a)

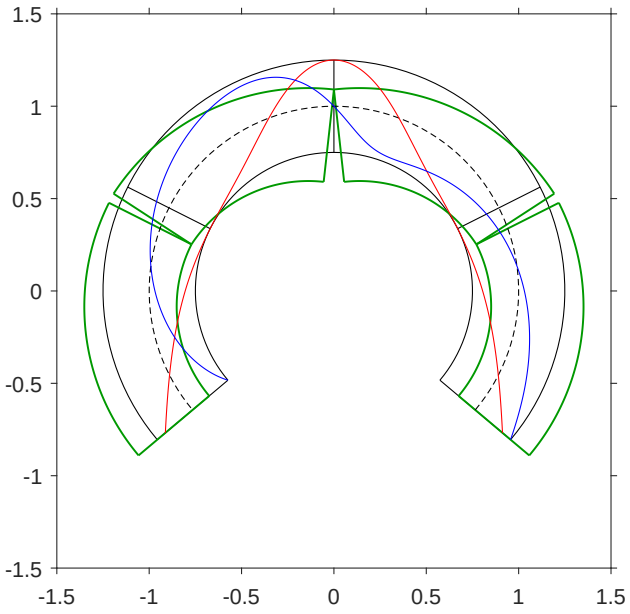

(b)

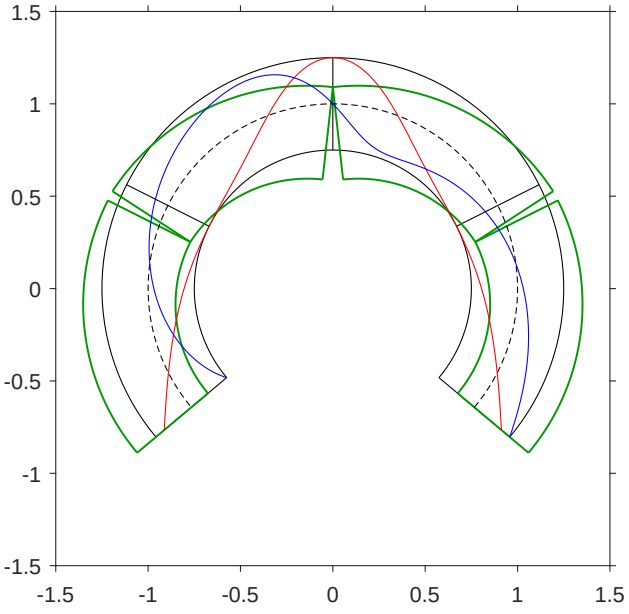

(c)

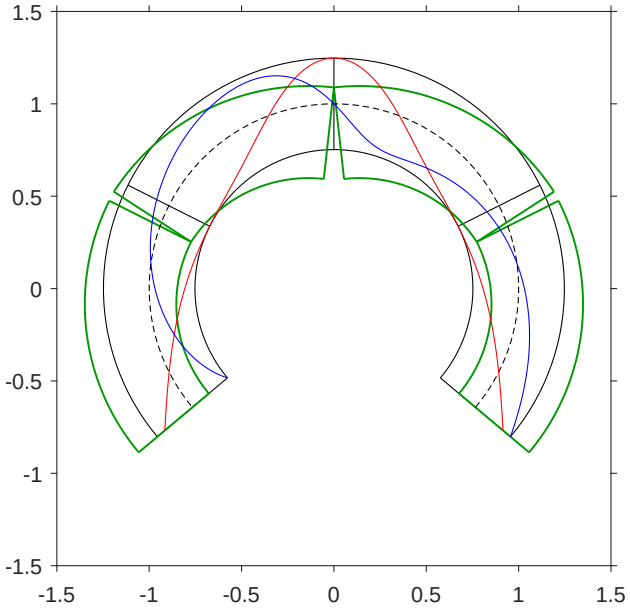

(d)

Figure 16: Arch reference configuration, with line of thrust and line of friction, and possible collapse mechanism. Reference state with $\eta = 0.5$, $\mu = 1.0$ ($\varphi = 45°$): (a) safe for $\alpha = 130°$; (b) SR collapse for $\alpha \simeq 130°$; (c) SR collapse with $\eta = 0.5$, $\mu \simeq 1$ and (d) SR collapse with $\eta \simeq 0.5$, $\mu = 1.0$ for $\alpha = 130°$. Characteristic values in Table 6 and itemized text.

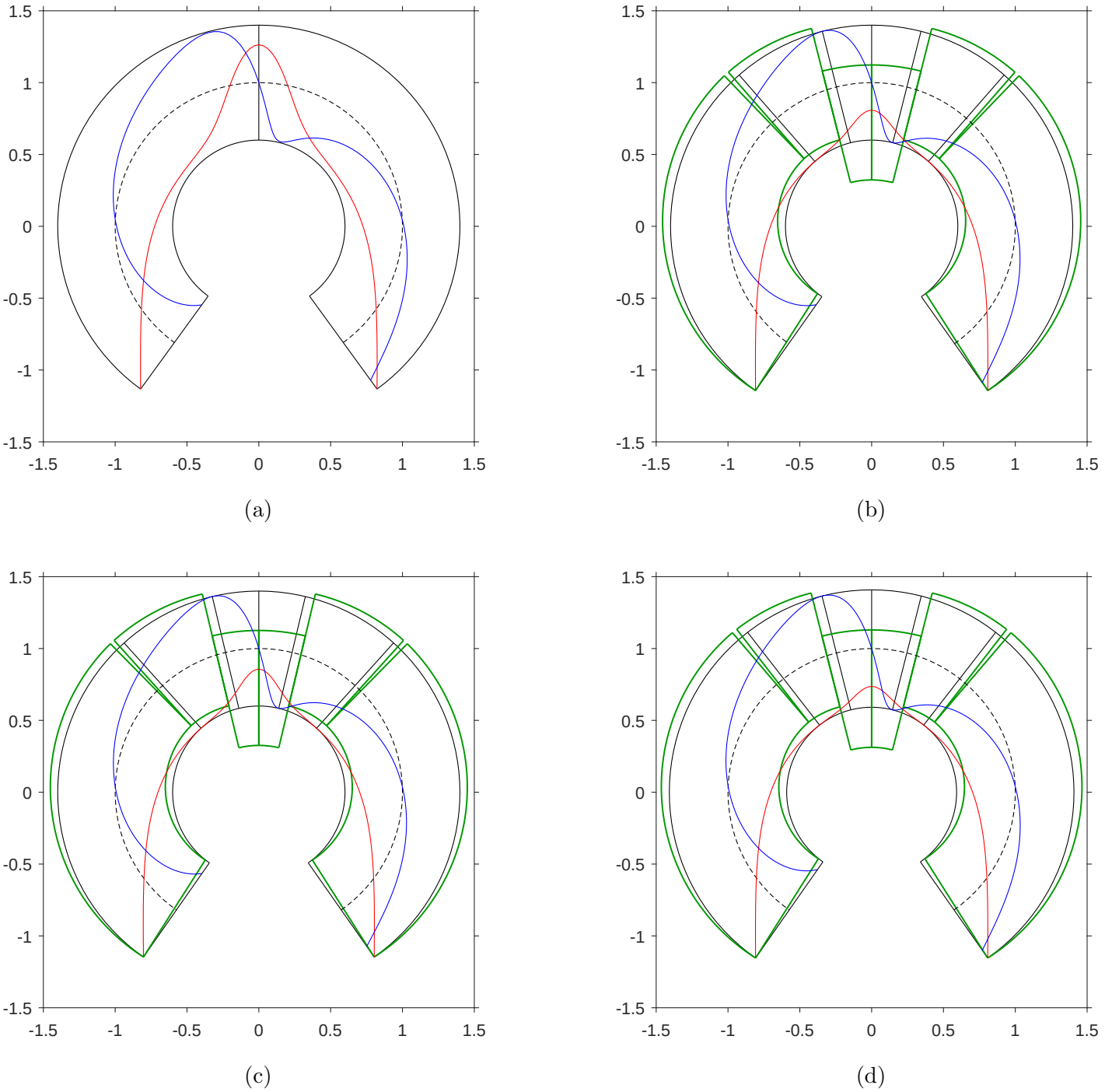

Figure 17: Arch reference configuration, with line of thrust and line of friction, and possible collapse mechanism. Reference state with $\eta = 0.8$, $\mu = 1.8$ ($\varphi \simeq 61°$): (a) safe for $\alpha = 144°$; (b) RS collapse for $\alpha \simeq 145°$; (c) RS collapse with $\eta = 0.8$, $\mu \simeq 1.8$ and (d) RS collapse with $\eta \simeq 0.8$, $\mu = 1.8$ for $\alpha = 145°$. Characteristic values in Table 7 and itemized text.